

# Unsynchronized evolution of salinity and pH of a Permian alkaline lake influenced by hydrothermal fluids: A multi-proxy geochemical study

Liuwen Xia<sup>1</sup>, Jian Cao<sup>1\*</sup>, Eva E. Stüeken<sup>2,3</sup>, Dongming Zhi<sup>4</sup>, Tingting Wang<sup>1</sup>, Wenwen Li<sup>1</sup>

1. State Key Laboratory of Mineral Deposits Research, School of Earth Sciences and Engineering, Nanjing University, Nanjing, Jiangsu 210023, China

2. School of Earth & Environmental Sciences, University of St Andrews, St Andrews KY16 9AL, Scotland, UK

3. NASA Astrobiology Institute, Virtual Planetary Laboratory, University of Washington, Seattle, WA 98195, USA

4. PetroChina Xinjiang Oilfield Company, Karamay, Xinjiang 843000, China

\* Corresponding author: Jian Cao. Email: jcao@nju.edu.cn; Tel: +86-25-87785973

Accepted by *Chemical Geology*, doi: 10.1016/j.chemgeo.2020.119581

## Abstract

Hyperalkaline waters display unusually high productivity, which makes them prime targets in the search for life elsewhere in the solar system. However, the formation mechanisms of alkaline waters are not well understood, because the response of biogeochemical proxies to these conditions is poorly constrained. To address this issue, we assessed the influence of hydrothermal fluids on the salinity and pH of alkaline lakes based on a case study of an early Permian paleo-alkaline lake (~290 Ma; Fengcheng Formation) in the Mahu Sag, northwestern Junggar Basin, China. Multiple proxies indicate that hydrothermal fluids in the central salt rock and marginal tuff–mudstone areas of the Fengcheng Formation were affected by deep and shallow hydrothermal fluids, respectively. A small part of the transitional area was affected by hydrothermal fluids with a hybrid nature. The hydrothermal fluid activity gradually weakened up-section in all areas while salinity (inferred from carbon and oxygen isotopes) increased and pH (inferred from nitrogen isotopes and mineralogy) decreased from hyperalkaline (> 9.25) to moderately alkaline conditions. These trends suggest that hyperalkalinity was largely driven by hydrothermal processes. In contrast, evaporation, which dominated towards the end of the lake's lifetime, maintained an elevated pH but did evidently not have a similarly strong effect as hydrothermal fluids. Our data suggest that hydrothermal activity and evaporation in closed lacustrine basins have the potential to create extreme conditions for the formation of alkaline lakes. The evolution of salinity and pH may not necessarily be synchronized.

**Keywords:** Alkaline soda lake; nitrogen isotopes; hydrothermal fluids; reedmergnerite; Junggar Basin; lower Permian Fengcheng Formation

## 1. Introduction

Alkaline lakes are typically characterized by  $\text{pH} > 9$ , high ratios of alkali metals (e.g.,  $\text{Na}^+$  and  $\text{K}^+$ ) to alkaline earth metals (e.g.,  $\text{Ca}^{2+}$  and  $\text{Mg}^{2+}$ ), and high  $\text{HCO}_3^-$  and  $\text{CO}_3^{2-}$  concentrations in the water column (Pecoraino et al., 2015). The high pH of soda lakes results not only from their high total alkalinity but also from the dominance of the monovalent cations,  $\text{Na}^+$  and  $\text{K}^+$ . In contrast, aqueous environments dominated by the divalent cation  $\text{Ca}^{2+}$  and  $\text{Mg}^{2+}$ , such as Dead Sea, are often characterized by relatively lower pH (Golan et al., 2016). Understanding the geological controls on these trends in water chemistry is of astrobiological significance as alkaline lakes host distinct microbial communities with unusually high biological productivity and may therefore be important geochemical archives of the evolution of life on Earth and other planetary bodies (Rothschild and Mancinelli, 2001; Stam et al., 2010; Rampelotto, 2013; Leboulanger et al., 2017).

Today, alkaline lakes tend to be most abundant in areas that are affected by recent volcanisms and located at relatively low latitudes with dry climates (Kempe and Kazmierczak, 2003). One of the major reasons behind this pattern is that water pH increases when fresh volcanic rock reacts with water during weathering at ambient temperature (Gislason and Eugster, 1987). Subsequent evaporation of these alkaline fluids that are derived from the weathering runoff of volcanic rocks raises pH further (Garrels and Mackenzie, 1967). Alkaline lakes are therefore usually also highly saline. However, it is conceivable that alkaline conditions are instead created by high-temperature processes. For example, serpentinization of ophiolites has been documented to create high-pH spring waters (Szponar et al., 2013). Hot springs are prevalent at the margins of Lake Magadi, an alkaline lake in the East African Rift (Renaut and Owen, 1988), but it remains unclear which process – low-temperature weathering or high-temperature water-rock reactions – has a stronger control on the development of alkaline lakes.

Reconstructions of pH from the rock record are most commonly undertaken by boron isotopic studies of carbonates, which can also constrain the atmospheric  $\text{CO}_2$  content in equilibrium with the water body (Vengosh et al., 1991). However, to apply this method it is necessary to determine both the  $\delta^{11}\text{B}$  of the carbonate and paleo-water. Given that seawater  $\delta^{11}\text{B}$  (39.6‰) has changed little since 10 Ma, this method is mainly applied to the reconstruction of ocean pH (Foster et al., 2010). In contrast,  $\delta^{11}\text{B}$  values of lake waters may vary significantly, prohibiting applications of this method to reconstructions of pH in ancient alkaline aquatic environments. An alternative proxy that may be more widely applicable are  $^{15}\text{N}/^{14}\text{N}$  ratios ( $\delta^{15}\text{N}$ ) of organic-rich sediments (Stüeken et al., 2015). With a  $\text{pK}_a$  of 9.25 at standard conditions, dissolved  $\text{NH}_4^+$  decomposes to  $\text{H}^+$  and  $\text{NH}_3$ . The loss of  $\text{NH}_3$  gas by volatilization leads to a  $\delta^{15}\text{N}$  fractionation of  $-45\%$ , raising the  $\delta^{15}\text{N}$  values of the remaining biomass and sediments (Li et al., 2012; Deng et al., 2018). Unlike boron, most nitrogen is sourced from the large atmospheric  $\text{N}_2$  reservoir, such that its source composition is usually close to 0‰. The process of biological nitrogen fixation has also been documented from alkaline hydrothermal fluids, where it is carried out by Archaea (Charlou et al., 2000; Mehta and Baross, 2006). Strongly elevated  $\delta^{15}\text{N}$  values typically characterize modern and ancient alkaline lacustrine environments (Stüeken et al., 2016). Although the quantitative relationship between  $\delta^{15}\text{N}$  and pH is not well understood, nitrogen isotopes can at least serve as a

qualitative proxy to distinguish between highly alkaline ( $\text{pH} > 9.25$ ) and circumneutral conditions. For example, the modern ocean with a pH of 8.2 does not show any alkalinity effect of  $\text{NH}_3$  volatilization, indicating that this process only becomes significant as higher pH values approaching and exceeding the  $\text{pK}_a$  of 9.25 where a large proportion of reduced nitrogen is present as  $\text{NH}_3$  rather than  $\text{NH}_4^+$  (e.g. Sigman et al., 2009).

In short, it is critical to reconstruct how biogeochemical proxies reflect and respond to the evolution of alkaline lakes in order to understand the formation of these habitats. Filling this knowledge gap is challenging as there are many interlinked factors. In this paper, we evaluated linkages between hydrothermal fluids, salinity and pH in a case study of the Junggar Basin, NW China, based on stratigraphic and lateral changes in geochemistry and mineralogy. This study also represents the first investigation of an alkaline lake in the Late Paleozoic worldwide.

## 2. Geological Setting

The Junggar Basin is located in the northern Xinjiang Uygur Autonomous Region of China. The basin has an area of  $1.3 \times 10^5 \text{ km}^2$  and hosts abundant oil and gas resources (Fig. 1; Carroll, 1998; Cao et al., 2005). Six sets of hydrocarbon source rocks are present, which are Carboniferous, Permian, Triassic, Jurassic, Cretaceous, and Paleogene in age (Cao et al., 2005). Alkaline lacustrine source rocks of the lower Permian Fengcheng Formation ( $\text{P}_{1f}$ ) mainly developed in Mahu Sag, which is located in the northern Central Depression.  $\text{P}_{1f}$  is further divided from base to top into the first ( $\text{P}_{1f1}$ ), second ( $\text{P}_{1f2}$ ), and third member ( $\text{P}_{1f3}$ ) (Figs. 1–2; Cao et al., 2005, 2015).

The Fengcheng Formation comprises typical alkaline lacustrine sediments containing wegscheiderite [ $\text{Na}_5\text{H}_3(\text{CO}_3)_4$ ], trona [ $\text{Na}_2\text{CO}_3 \cdot \text{NaHCO}_3 \cdot 2\text{H}_2\text{O}$ ], nahcolite [ $\text{NaHCO}_3$ ], shortite [ $\text{Na}_2\text{Ca}_2(\text{CO}_3)_3$ ], northupite [ $\text{MgCO}_3 \cdot \text{Na}_2\text{CO}_3 \cdot \text{NaCl}$ ], and eitelite [ $\text{Na}_2\text{Mg}_2(\text{CO}_3)_3$ ] (Cao et al., 2015, 2020). The sedimentary succession reveals five stages in the evolution of the lake; i.e., the early onset, preliminary, strong, weak, and terminal alkalinity stages. The mineral evidence for an alkaline lake includes the presence of trona, nahcolite, and wegscheiderite. Abundant pyrite further indicates a reducing environment, consistent with a highly productive ecosystem. Geochemical evidence for an alkaline lake includes biomarkers characterized by pristane/phytane  $< 1$ , high abundances of carotane, gammacerane index values (gammacerane/ $\text{C}_{30}$  hopane) of  $>0.3$ , and tricyclic terpane abundances in the order  $\text{C}_{20} < \text{C}_{21} < \text{C}_{22}$ . Based on these observations, Cao et al. (2015) proposed that a complete alkaline lacustrine evolutionary cycle characterized  $\text{P}_{1f1}$  to  $\text{P}_{1f3}$ , and that  $\text{P}_{1f2}$  was deposited under the most alkaline conditions with the highest carbonate contents.

The Fengcheng Formation was deposited in a post-orogenic, extensional fault depression that developed on Paleozoic basement in the western Junggar Basin. The formation comprises fan delta and lake sediments. The alkaline lacustrine sediments were deposited mainly in the center of Mahu Sag (Cao et al., 2015). We divided the Fengcheng Formation in Mahu Sag into three areas: (1) a central lake area with large amounts of deposition of alkali minerals; (2) a transitional area dominated by dolomites; and (3) a marginal area dominated by tuffs and mudstones. These three areas are termed the central salt rock (CSR), transitional dolomite (TD), and marginal tuff–mudstone (MTM) areas, respectively (Fig. 3).

### 3. Samples and Methods

#### 3.1 Samples

To explore the effects of hydrothermal fluids on the salinity of an alkaline lake, we collected 56 samples from the Fengcheng Formation in Mahu Sag, including 28 samples from four cores (F20, FN5, FN7, and AK1) in the CSR, 17 samples from three cores (F5, FN1, and FN14) in the TD, and 11 samples from four cores (X40, X76, BQ1, and B26) in the MTM (Figs 1 and 3). Twenty-seven, 19, and 10 samples were taken of P<sub>1f3</sub>, P<sub>1f2</sub>, and P<sub>1f1</sub>, respectively. As successive core samples are not available due to drilling cost, we built composite sections from adjacent cores for compensation. For example, samples from F20, FN5, FN7, and AK1 wells were used jointly to reflect the characteristics of CSR and samples from FN1, FN14, and F5 wells were combined to reflect the characteristics of TD.

#### 3.2 Methods

##### 3.2.1 Mineralogy

Optical microscopy, scanning electron microscopy and energy dispersive spectrometry (SEM–EDS), and electron probe microanalysis (EPMA) were undertaken at the School of Earth Sciences and Engineering, Nanjing University, Nanjing, China. For optical microscopy, rock samples were sectioned vertically, embedded in a mixture of epoxy resin and hardener (ratio of 5:1), and polished. The resulting thin-sections were examined under plane- and cross-polarized light with a Nikon optical microscope.

For SEM–EDS analysis, we used air-dried samples that were mounted on stubs using double-sided adhesive tape, which were then coated with Pt–Pd using a Polaron E5000 sputter coater at 1.2 kV for 2 × 2 min. The SEM analyses were conducted with a JSM-6490 instrument operated at an accelerating voltage of 15.0 kV and a beam current of 1.0–2.0 × 10<sup>-9</sup> A. Semi-quantitative elemental analysis was carried out using an X-ray energy dispersive spectrometer.

Thin-sections were carbon-coated and back-scattered electron imaging (BEI) and mineral analyses were performed on these with a JEOL JXA8800M EPMA. Matrix corrections were based on ZAF procedures. The EPMA was operated at an accelerating voltage of 20 kV with a 5 × 10<sup>-9</sup> A beam current for BEI, and an accelerating voltage of 20 kV with a 2 × 10<sup>-8</sup> A beam current for quantitative analysis.

##### 3.2.2 Geochemistry

The samples were subjected to inductively coupled plasma–mass spectrometry (ICP–MS) trace element analysis, carbonate C–O stable isotopic analysis, determination of total N–S–C contents, and total N and organic C stable isotopic analysis. ICP–MS and C–O stable isotopic analyses were conducted at the School of Earth Sciences and Engineering, Nanjing University, Nanjing, China. N–S–C contents and total N and organic C stable isotopic data were determined at the School of Earth and Environmental Sciences, University of St Andrews, Scotland, United Kingdom.

Trace elements were determined with an Elan DRC-e ICP–MS. Firstly, 0.05 g of sample powder (< 200 mesh), 0.5 mL of concentrated HF, and 1 mL of concentrated HNO<sub>3</sub> were placed in sealed Teflon beakers and heated at 185°C for 12 h. The samples were cooled and

then evaporated to dryness. After addition of 1 mL of concentrated HNO<sub>3</sub>, the samples were again evaporated to dryness. Subsequently, 2 mL of dilute HNO<sub>3</sub>, 1 mL of 500 ng/mL Rh internal standard, and 3 mL of H<sub>2</sub>O were added. The mixture was then sealed and heated at 140°C for 5 h. After cooling, 0.4 mL of the solution was placed in a 15 mL centrifuge tube, sealed, and heated at 140°C for 5 h. This solution was then diluted to 8–10 mL with distilled deionized water. Finally, the sample was analyzed by ICP–MS using the Rh internal standard method. Europium anomalies in rare earth element (REE) patterns normalized to Post-Archean Australian Shale (PAAS) were calculated as follows:  $Eu/Eu^* = 2Eu_N / (Sm_N + Gd_N)$ . Here  $Eu_N$ ,  $Sm_N$ , and  $Gd_N$  denote relative Eu, Sm and Gd abundances after normalization to Post-Archean Australian Shale (PAAS).

For carbonate stable C–O isotopic analysis, powdered samples (< 200 mesh) were immersed in dilute H<sub>2</sub>O<sub>2</sub> for 72 h to oxidize the organic C in the samples. Subsequently, 20 mg of the centrifuged, dried powder was reacted with 100% H<sub>3</sub>PO<sub>4</sub> at 25°C for 12 h, and a liquid N<sub>2</sub> trap was used to collect pure CO<sub>2</sub>. The resulting CO<sub>2</sub> was analyzed with a MAT253 mass spectrometer to obtain <sup>13</sup>C/<sup>12</sup>C and <sup>18</sup>O/<sup>16</sup>O ratios. Both  $\delta^{13}C_{carb}$  and  $\delta^{18}O_{carb}$  are expressed in delta notation relative to V-PDB:  $\delta [‰] = ({}^{x/y}R_{sample}/{}^{x/y}R_{standard} - 1)$ , where  ${}^{x/y}R = {}^{18}O/{}^{16}O$  for O and  ${}^{13}C/{}^{12}C$  for C.

For analysis of the total N–S–C contents, total N stable isotopes, and organic C stable isotopes, 6 N HCl was added to the dried sample powders (<200 mesh) at 25°C overnight to remove carbonates. The resulting samples were washed three times with 18 MΩ H<sub>2</sub>O, and then dried in an oven overnight. Decarbonated powders were weighed into Sn capsules and analyzed by flash combustion in an elemental analyzer (EA Isolink) coupled to an isotope ratio mass spectrometer (Thermo Finnigan MAT253). We used USGS40, USGS41, and SGR1 as in-house standards. The isotopic data are expressed in delta notation relative to V-PDB for  $\delta^{13}C_{org}$  and relative to air for  $\delta^{15}N$ :  $\delta [‰] = ({}^{x/y}R_{sample}/{}^{x/y}R_{standard} - 1)$ , where  ${}^{x/y}R = {}^{15}N/{}^{14}N$  for N and  ${}^{13}C/{}^{12}C$  for C. Precision and accuracy based on SGR-1 were better than 0.5 ‰ for both carbon and nitrogen isotopes.

## 4. Results

### 4.1. Hydrothermal fluids

Typical indicators of the former presence of hydrothermal fluids include the mineral reedmergnerite (Wunder et al., 2013) and Eu anomalies (Humphris and Bach, 2005). Reedmergnerite (NaBSi<sub>3</sub>O<sub>8</sub>) is a transparent wedge-shaped and aggregated platy mineral under plane-polarized light, with first-order gray to yellow interference colors under cross-polarized light (Fig. 4). Abundant, sparse, and no reedmergnerite were found in the Fengcheng Formation of the CSR, TD, and MTM, respectively. The abundance of reedmergnerite gradually decreases up-section from P<sub>1</sub>f<sub>1</sub> to P<sub>1</sub>f<sub>3</sub>.

Positive europium anomalies in the CSR, MTM, and TD vary from large to small, respectively, and also gradually decrease up-section from P<sub>1</sub>f<sub>1</sub> to P<sub>1</sub>f<sub>3</sub> (Table 1).

### 4.2. Salinity

We tested a range of proposed paleo-salinity proxies including the Z-value and  $\delta^{18}O_{carb}$  (Keith and Weber, 1964; Polyak et al., 2003; Liu et al., 2009; Yu et al., 2018), TOC/TS and

Y/Ho ratios. In detail, the Z-value is defined as  $2.048 \times (\delta^{13}\text{C}_{\text{carb}} + 50) + 0.498 \times (\delta^{18}\text{O}_{\text{carb}} + 50)$ , which has been extensively applied in the study of post-Triassic environments to distinguish marine from freshwater settings based on an empirically defined threshold of 120 (i.e., marine > 120 and freshwater lacustrine < 120; Keith and Weber, 1964). In pre-Triassic environments, a specific salinity threshold has so far not been defined, but both parameters can still be used to reconstruct *relative* vertical and horizontal variations in salinity (Keith and Weber, 1964). Fundamentally, both  $\delta^{18}\text{O}_{\text{carb}}$  and  $\delta^{13}\text{C}_{\text{carb}}$  (and hence the Z-value) have been shown to increase with salinity because isotopically light  $\text{H}_2\text{O}$  and  $\text{CO}_2$  are lost preferentially during evaporation. In contrast, TOC/TS ratios are expected to decrease with increasing salinity if saline waters contain higher abundances of sulfate, leading to sulfide enrichments relative to organic carbon in anoxic sediments. Y/Ho ratios of chemical sediments such as carbonates are elevated in saline waters due to preferential stabilization of Y by anionic salts. It is important to note that the Y/Ho proxy was first defined in marine systems where the salinity effects take control within estuaries (Lawrence and Kamber, 2006). In relatively smaller lake basins, it is conceivable that kinetic barriers make this proxy less precise. Sr/Ba was not used as a salinity proxy in this study as the high content of carbonates of our samples (up to over 90%) may contribute excess amounts of carbonate-bound Sr (Freitas et al., 2006). Also, we did not use B/Ga and the Couch formula as salinity proxies (Degens et al., 1957; Couch, 1971), because the presence of reedmergnerite is evidence for strong hydrothermal addition of boron into the lake basin, which would compromise the utility of this proxy.

Results show that salinity varied significantly, both laterally and up-section in the Fengcheng Formation. Laterally, Z-values and Y/Ho ratios exhibit the following trend: TD > CSR > MTM. The  $\delta^{18}\text{O}_{\text{carb}}$  values and TOC/TS ratios exhibit a trend of CSR > TD > MTM, and MTM > CSR > TD, respectively (Fig. 3). Moving up-section from P<sub>1</sub>f<sub>1</sub> to P<sub>1</sub>f<sub>3</sub>, Z-values,  $\delta^{18}\text{O}_{\text{carb}}$  values, and TOC/TS ratios gradually increase, whereas Y/Ho ratios gradually decrease (Table 2).

### 4.3. pH

The pH proxy used in this study was based mainly on  $\delta^{15}\text{N}$  values. Ratios of organic carbon to nitrogen (molar C/N) and  $\delta^{13}\text{C}_{\text{org}}$  values can provide additional constraints when using  $\delta^{15}\text{N}$  as a pH proxy (discussed below).  $\delta^{15}\text{N}$  values of the CSR and TD are similar and higher than those of the MTM. All values exceed 10‰ and are thus higher than the vast majority of marine sediments and freshwater lakes, which display modes around 4-6‰ (Tesdal et al., 2013) and 2-3‰ (McLauchlan et al. 2013), respectively. Molar C/N values exhibit a trend of CSR > TD > MTM.  $\delta^{13}\text{C}_{\text{org}}$  values in these three areas are similar. Moving up-section, from P<sub>1</sub>f<sub>1</sub> to P<sub>1</sub>f<sub>3</sub>, C/N first increases and then decreases, whereas  $\delta^{15}\text{N}$  and  $\delta^{13}\text{C}_{\text{org}}$  values gradually decrease (Fig. 3; Table 3).

## 5. Discussion

### 5.1. Effects of diagenesis and lithology

To ensure reliability of our data, diagenetic alteration and lithological effects of the proxies should be addressed. As for  $\delta^{13}\text{C}_{\text{carb}}$  and  $\delta^{18}\text{O}_{\text{carb}}$  values, there is no evidence of diagenetic alteration, based on the absence of correlations between  $\delta^{13}\text{C}_{\text{carb}}$ ,  $\delta^{18}\text{O}_{\text{carb}}$ , TOC and carbonate

contents, and Mn/Sr < 10 (Figs. 5a–5e; Kaufman and Knoll, 1995; Stüeken and Buick, 2017). For samples of Fengcheng Formation, the increasing carbonate contents indicates a lithological transition from mudstones or tuffs to carbonates. As there is no correlation between  $\delta^{13}\text{C}_{\text{carb}}$ ,  $\delta^{18}\text{O}_{\text{carb}}$  and carbonate contents (Figs. 5d–5e), petrological control on these values can be ignored. Furthermore,  $\delta^{13}\text{C}$  values from carbonates and organic matter are not correlated (Fig. 5f), which would be the case if extensive diagenetic oxidation of organic matter had led to the formation of significant amounts of diagenetic carbonate.

Regarding nitrogen, early diagenesis is responsible for releasing organic nitrogen into the water column, where it undergoes isotopic fractionation in response to environmental conditions. Diagenesis is therefore an integral part of the nitrogen cycle. However, diagenetic pathways are controlled by environmental conditions and can still record primary information. For example, remineralization of organic nitrogen would be sensitive to the influence of alkaline waters in the lake, which are in turn sourced from deep hydrothermal fluids, i.e. the same fluids influencing conditions of the depositional environment. It is unlikely that extremely alkaline conditions (pH > 9) would be established by early diagenesis alone, because during this stage the composition of pore waters would still be in exchange with the overlying lake. Nitrogen isotope evidence of high alkalinity therefore most likely reflects high alkalinity in the depositional environment, from where it translated into early diagenetic pore fluids. If early diagenesis were to occur under influence of a non-alkaline fluid, the final  $\delta^{15}\text{N}$  value would not be as high as recorded in the rocks. Our data thus require consistently alkaline conditions. Another process that can perturb nitrogen isotopes is regional metamorphism above lower greenschist facies (e.g. Haendel et al., 1986). However, the preservation of oil shale in this setting is evidence for a very low regional metamorphic grade, where this process is negligible. Contact metamorphism or heating by hydrothermal fluids could have occurred, but as noted below, the presence of Na-carbonates, which are unstable above 40°C, points towards low temperatures. Furthermore, we do not see evidence for a lithological control on our nitrogen isotope data (Fig. 6). In Fengcheng alkaline sediments, TN and TOC, both decarbonated, are strongly correlated ( $R^2 = 0.75$ , Fig. 6a), indicating that most nitrogen is derived from primary organic matter rather than from detrital clay minerals. This correlation also rules out significant input of exogenous ammonium by hydrothermal fluids. And input of detrital plant material appears to be negligible, based on organic carbon isotopes. Hence, similar to  $\delta^{13}\text{C}_{\text{carb}}$  and  $\delta^{18}\text{O}_{\text{carb}}$  values, the TN and  $\delta^{15}\text{N}$  data most likely reflect primary and early diagenetic processes that were controlled by environmental conditions during the time of deposition (Figs. 6e–6f). The effects of diagenesis and lithology on trace element parameters such as Eu/Eu\* and Y/Ho are also addressed in similar way (Fig. 7). As there are no obvious correlations between Eu/Eu\*, Y/Ho, TOC and carbonate contents (Fig. 7), impacts of diagenesis and lithology on Eu/Eu\* and Y/Ho values are negligible.

## 5.2. Hydrothermal fluids in an alkaline lake

The proxies used in this study to assess the role of hydrothermal fluids were the absence/presence of reedmergnerite and Eu anomalies (Bau and Dulski, 1996; Noll et al., 1996; Humphris and Bach, 2005). Boron from deep hydrothermal fluids can replace Si in albite ( $\text{NaAlSi}_3\text{O}_8$ ) to form reedmergnerite ( $\text{NaAlB}_3\text{O}_8$ ) (Noll et al., 1996; Wunder et al., 2013). In this study, reedmergnerite was found in the CSR (>60% of samples), the TD (>30%

of samples), but not in the MTM, reflecting a diminishing role for deep hydrothermal fluids moving through each of these areas.

Positive Eu anomalies with  $\text{Eu}/\text{Eu}^* > 1.05$  are often interpreted as evidence of hydrothermal fluids that were hot enough ( $>200^\circ\text{C}$ ) to facilitate the reduction of  $\text{Eu}^{3+}$  to  $\text{Eu}^{2+}$  (Bau and Dulski, 1996). Also depletion in light REE (LREE) is typical of the influence of deep hydrothermal fluids (Noll et al., 1996; Humphris and Bach, 2005). Alternatively, LREE depletion may indicate high pH, as reported from modern alkaline lakes, where carbonate ions stabilize heavy REE (HREE) in solution (Möller and Bau, 1993). In the case of Mahu Sag, it is important to note that the basin is floored by Early Carboniferous alkali olivine-rich basalts that are characterized by  $\text{Eu}/\text{Eu}^* = 1.82$  and LREE depletion (Fig. 8; Zeng et al., 2002; Zhang et al., 2006). Hence, it is possible that the REE patterns and positive Eu anomalies observed in our samples (Table 1) reflect simple weathering or erosion of this basalt rather than high-temperature hydrothermal fluids and pH effects. However, later volcanic eruptions during the deposition of P<sub>1f</sub> emplaced rhyolite and/or andesite in Mahu Sag with  $\text{Eu}/\text{Eu}^* = 0.82 \pm 0.16$  and flat REE patterns (Fig. 8; Chang et al., 2016). To explain the observed spatial trends in our data, a strong weathering influence by the older Carboniferous basalts would thus require (1) upward migration of deep-seated cold fluids, and (2) relatively higher degrees of basalt weathering in the CSR compared to the lake margins. Point (2) seems unlikely, and although point (1) is possible, upward fluid migration would be greatly facilitated by heating. Paired with the high abundance of reedmergnerite in the central lake samples, which is an indicator of deep hydrothermal input, we therefore conclude that the large positive Eu anomalies in the CSR reflect a significant influence of hydrothermal fluids. Along the lake margins, where Eu anomalies are smaller and reedmergnerite abundances much lower, hydrothermal fluids may have been absent, or – if present – characterized by much lower temperatures than in the lake center. The flat REE patterns in these samples likely reflect rhyolite/andesite weathering.

### 5.3. Salinity and hydrothermal influences on the Fengcheng Formation in the Mahu Sag

#### 5.3.1. Z-values and $\delta^{18}\text{O}_{\text{carb}}$ values

The Z-values and  $\delta^{18}\text{O}_{\text{carb}}$  values suggest that salinity generally decreased from the CSR (relatively medium to high salinity) to the TD (relatively low to high salinity) and to the MTM (relatively low to medium salinity) (Fig. 3). Moving up-section, in the CSR and TD, salinity appears to have gradually increased (Figs. 9 and 10), which would indicate progressive evaporation of the basin. It is noteworthy that there may have been an equilibrium fractionation in  $\delta^{18}\text{O}_{\text{carb}}$  between different co-precipitating carbonate minerals of P<sub>1f</sub> in the Mahu Sag including calcite, dolomite, trona, nahcolite, wegscheiderite, shortite and northupite (O’Neil et al., 1966; Yu et al., 2018). For example, the equilibrium fractionation in  $\delta^{18}\text{O}_{\text{carb}}$  between dolomite and calcite is around 0–1‰ (O’Neil et al., 1966). For other types of carbonates in the study area the equilibrium fractionation factor remains unknown, but it is unlikely that this effect can explain the large range of over 15‰ in our  $\delta^{18}\text{O}_{\text{carb}}$  data. Therefore, most of the signal likely reflects changes in the composition of the fluid.

The lack of correlation with  $\text{Eu}/\text{Eu}^*$  shows that the hydrothermal fluids have little or no effect on these salinity indicators. Z-values and  $\delta^{18}\text{O}_{\text{carb}}$  values in the CSR exhibit only a weak negative correlation with  $\text{Eu}/\text{Eu}^*$  ( $R^2 = 0.23$  and  $0.15$ , respectively) (Fig. 11a–b), which may

reflect mild modification of the salinity proxies by deep hydrothermal fluids that are enriched in isotopically light  $\text{HCO}_3^-$  and/or  $\text{CO}_3^{2-}$  and thus lowering of Z-values and  $\delta^{18}\text{O}_{\text{carb}}$  values. According to Zheng and Hoefs (1993), both  $\delta^{13}\text{C}_{\text{carb}}$  and  $\delta^{18}\text{O}_{\text{carb}}$  in deep hydrothermal fluids are isotopically light ( $\delta^{13}\text{C}_{\text{carb}} = -7\text{‰}$  and  $\delta^{18}\text{O}_{\text{carb}} = -23.2\text{‰}$ ). However, the weak correlation with Eu anomalies suggests that this effect was minor. Data from the TD and MTM show no correlations between Z-values or  $\delta^{18}\text{O}_{\text{carb}}$  values and Eu/Eu\*, indicating that hydrothermal fluids in these two areas – if present – had no effect on Z-values and  $\delta^{18}\text{O}_{\text{carb}}$  values (Fig. 11c–d). In summary, Z-values and  $\delta^{18}\text{O}_{\text{carb}}$  values probably reflect salinity robustly in this setting.

### 5.3.2. TOC/TS ratios

TOC/TS ratios are also a water salinity proxy, because sulfate concentrations of water vary from an average of 10 ppm in freshwater lakes to an average of 2900 ppm in the modern ocean, and to >20,000 ppm in closed and saline lakes (Bernier and Raiswell, 1984; Yao and Millero, 1996). Wei and Algeo (2019) distinguished freshwater and seawater using the ratio of TOC to sulfur in sedimentary rocks: TOC/TS < 5 indicates seawater or saltwater, TOC/TS > 10 indicates freshwater, and TOC/TS = 5–10 indicates saline to brackish water (Wei et al., 2018; Bernier and Raiswell, 1984). In this study, the lateral variations in salinity indicated by TOC/TS ratios are complex. According to this proxy, the CSR would have been dominated by freshwater–saltwater, and the TD and MTM would have the highest and lowest salinity, respectively (Fig. 12). Furthermore, TOC/TS ratios suggest that the salinity of the CSR and TD gradually decreased up-section (Figs. 9 and 10).

These observations conflict with the Z-values and  $\delta^{18}\text{O}_{\text{carb}}$  values, which are based on carbon and oxygen isotopes. It is conceivable that these proxies record the chemistry of different layers in a salinity-stratified water column (Stüeken et al., 2019).  $\delta^{13}\text{C}_{\text{carb}}$  and  $\delta^{18}\text{O}_{\text{carb}}$  values may reflect the relatively fresher and better-mixed surface waters (Reghellin et al., 2015), whereas TOC/TS ratios reflect the pyrite and organic sulfur in bottom waters and a benthic setting (Diamond et al., 2018). In our case, the Z-values and  $\delta^{18}\text{O}_{\text{carb}}$  values would thus indicate that the salinity of the surface water gradually increased from P<sub>1f1</sub> to P<sub>1f3</sub>, whereas the TOC/TS ratios indicate that the salinity of the bottom water gradually decreased from P<sub>1f1</sub> to P<sub>1f3</sub>. However, this scenario seems unlikely, because saline waters are dense and would tend to sink to the bottom. For example, Stüeken et al. (2019) found that the salinity recorded by  $\delta^{13}\text{C}_{\text{carb}}$  and  $\delta^{18}\text{O}_{\text{carb}}$  indicates relatively fresher surface waters and is opposite to the salinity recorded by organic geochemical proxies in paleo-alkaline lake sediments of the Jurassic Towaco Formation in the Newark Basin, eastern USA.

The discrepancy between the two proxies is probably best explained by the addition of either organic carbon or reduced sulfur in different intervals. Elevated TOC/TS ratios may be due to elevated primary productivity that added organic carbon to the saline facies. Alternatively, hydrothermal fluids may have added sulfur. Hydrothermal fluids often contain H<sub>2</sub>S (Arp and Childress, 1983; Hedenquist and Lowenstern, 1994), which could have led to pyrite enrichments, independent of the local organic carbon burial flux (Arp and Childress, 1983; Diamond et al., 2018). To test this possibility, plots between TOC/TS and Eu/Eu\* were examined (Fig. 12). These plots suggest that the hydrothermal fluids in the CSR area significantly decreased TOC/TS ratios, whereas the hydrothermal fluids in the TD and MTM had no significant effect. When Eu/Eu\* < 1.1 in the CSR, TOC/TS ratios decrease rapidly

with increasing  $\text{Eu}/\text{Eu}^*$ , but when  $\text{Eu}/\text{Eu}^* > 1.1$ , TOC/TS ratios remain at a constant low value (Fig. 12a). These trends point to strong hydrothermal overprint of TOC/TS ratios; they can therefore only serve as salinity indicators if hydrothermal input is absent or at least very low (Fig. 12a).

**5.3.3. Y/Ho ratios** Yttrium is more strongly stabilized by anionic complexes than Ho, causing Ho to adsorb more readily to particles such as ferric hydroxides. Holmium is thus scavenged from the water column in estuaries, which leads to much higher Y/Ho ratios in seawater compared to freshwater, and positive correlations between Y/Ho ratios and salinity (Lawrence and Kamber, 2006). However, Y/Ho ratios are also affected by factors other than salinity, such as ferric hydroxide contents (Lawrence and Kamber, 2006). As a result, this proxy is not always sensitive to changes in salinity (Wei et al., 2018).

In the present study, Y/Ho ratios were not useful paleo-salinity proxies. Although plots of Y/Ho and  $\text{Eu}/\text{Eu}^*$  (Figs. 12b and 12d) show only a weak positive correlation between Y/Ho and  $\text{Eu}/\text{Eu}^*$  in the CSR ( $R^2 = 0.12$ ), both Y/Ho and  $\text{Eu}/\text{Eu}^*$  gradually decrease from P<sub>1f1</sub> to P<sub>1f3</sub> (Fig. 9). At face value, this pattern would imply that the deep hydrothermal fluids in the CSR slightly increased salinity, (Fig. 12b), counter to what we inferred from Z-values and  $\delta^{18}\text{O}_{\text{carb}}$  values (see above). This discrepancy may be attributable to deep hydrothermal fluids introducing heavy rare earth elements and Y, which thus slightly increases Y/Ho ratios (Humphris and Bach, 2005; Sugitani et al., 2006). The other sampling sites do not show any correlation between Y/Ho and  $\text{Eu}/\text{Eu}^*$ , (Fig. 12d), possibly due to the weak influence of hydrothermal fluids in these areas.

#### **5.3.4. Salinity evolution in space and time**

Based on the above discussion, Z-values and  $\delta^{18}\text{O}_{\text{carb}}$  values best record the true water salinity of the Fengcheng Formation.

The salinity of the CSR is higher than that of the TD and MTM, probably reflecting mild dilution by freshwater along the lake margins. The salinity also gradually increases up-section, which may reflect an increasingly arid climate (Fig. 2). This interpretation would be consistent with the late Carboniferous–late Permian northward drift of the Pangaea supercontinent, in which Mahu Sag was located, and gradual closure of the Panthalassic Ocean between Laurussia and Gondwana (Roscher and Schneider, 2006). The salinity variations in the Fengcheng Formation (see Section 5.1) were controlled mainly by the drying paleoclimate.

## **5.4. pH and hydrothermal fluids**

### **5.4.1. pH**

Nitrogen in sediments is often used to trace the redox state of the overlying water column and the prevalence of certain biological metabolisms (Quan et al., 2013; Ader et al., 2016; Stüeken et al., 2016). The main form of nitrogen in the oxidized modern ocean is  $\text{NO}_3^-$  with a  $\delta^{15}\text{N}$  value of about +5‰, and the main forms of nitrogen in the reducing early–middle Archean ocean was  $\text{NH}_4^+$  with a  $\delta^{15}\text{N}$  value of ~0‰ (Sigman et al., 2009). The difference between the modern oxidized and Archean reducing oceans is due mainly to isotopic fractionation caused by denitrification in suboxic environments (Sigman et al., 2009). During

nitrification,  $\text{NH}_4^+$  is rapidly oxidized to  $\text{NO}_2^-$  and then to  $\text{NO}_3^-$  without net fractionation between nitrogen isotopes, but when the resulting  $\text{NO}_3^-$  encounters sub-oxic conditions in oxygen minimum zones, some of it gets reduced to  $\text{N}_2$  by biological denitrifiers. This process preferentially consumes  $^{14}\text{N}$ , making the  $\delta^{15}\text{N}$  value of the remaining  $\text{NO}_3^-$  heavier. This signature is then transferred to sediments when organisms consume the heavy  $\text{NO}_3^-$  as a nutrient without significant net isotopic effect (Freudenthal et al., 2001; Ader et al., 2016). However, in highly alkaline lakes,  $\delta^{15}\text{N}$  can be extremely heavy, including in modern and Archean alkaline lakes (mean 13.7‰ and 31.9‰, respectively; Griffin et al., 2007; McLauchlan et al., 2013; Stüeken et al., 2015). The extremely heavy  $\delta^{15}\text{N}$  values of alkaline lakes are too large to be solely the result of redox processes and are most parsimoniously explained by  $\text{NH}_3$  volatilization under alkaline and reducing conditions (Li et al., 2012; Stüeken et al., 2015; Stüeken et al., 2019). With a pKa of 9.25,  $\text{NH}_4^+$  is converted to  $\text{H}^+$  and  $\text{NH}_3$ .  $\text{NH}_3$  is volatile and escapes into the atmosphere while the remaining  $^{15}\text{N}$ -rich  $\text{NH}_4^+$  is stored in biomass and sediments (Talbot and Johannessen, 1992; Stüeken et al., 2016). Strongly reducing conditions probably favor this process, because such conditions inhibit the oxidation of  $\text{NH}_4^+/\text{NH}_3$  prior to volatilization.

$\delta^{15}\text{N}$  values of the Fengcheng Formation are extremely heavy, with an average of +18.9‰ and a maximum of +24.4‰, which are much higher than average  $\delta^{15}\text{N}$  values of +3‰ in modern lakes (Fig. 13; McLauchlan et al., 2013). Given the co-occurrence of Na-rich carbonates, which are typically encountered in strongly evaporitic alkaline lakes, these values most likely reflect a high pH > 9.25 in the lake during the time of deposition. Also the organic biomarkers, which are often used to indicate salinity and redox conditions (Peters et al., 2005) are consistent with the high pH values indicated by  $\delta^{15}\text{N}$ , because these particular biomarker signatures are often found in alkaline settings. The mineralogical assemblages in Mahu Sag have previously been interpreted as reflecting five distinct stages of alkalization (Cao et al., 2015; Pecoraino et al., 2015): (i) the early onset (Mg–Ca carbonates calcite and dolomite), (ii) preliminary (Mg–Ca carbonates and occurrence of transitional carbonates including shortite, northupite, and eitelite), (iii) strong (abundant Na carbonates including trona, nahcolite, and wegscheiderite), (iv) weak (disappearance of Na carbonates), and (v) terminal alkalinity (return to pure Mg–Ca carbonates). For our studied intervals, these stages are listed in Table 4. This compilation shows that nitrogen isotope values only exceed 18‰ when Na-bearing carbonates are present, but the highest values (>22‰) occur in the basal part of the CSR, where hydrothermal fluid input was most noticeable, rather than in the most saline sections that contain the highest abundance of Na-carbonates. Hence, hydrothermal fluids appear to have had a stronger influence than water column evaporation on elevating nitrogen isotope ratios by driving  $\text{NH}_3$  volatilization.

$\text{NH}_3$  loss is further supported by C/N ratios. The Fengcheng Formation has high C/N ratios with an average value of 39.5 and a maximum of 75.33, which are much higher than the C/N ratios of fresh marine black shales (7–10; Godfrey and Glass, 2011). This might reflect either the input of large amounts of C from terrestrial organic matter or N loss. The former is unlikely because the high C/N ratios of the Fengcheng Formation coincide with light  $\delta^{13}\text{C}_{\text{org}}$ , with an average of –27.6‰. According to Arthur et al. (1985), organic matter with  $\delta^{13}\text{C}_{\text{org}}$  of –29‰ to –27‰ mainly comes from lower aquatic organisms, while organic matter with  $\delta^{13}\text{C}_{\text{org}}$  of –25‰ to –24‰ is derived mainly from terrestrial higher plants. Therefore, the high C/N

ratios are incompatible with plant biomass and most likely reflect enhanced nitrogen loss during NH<sub>3</sub> release. In conclusion, the pH of the water column was probably close to or above 9.25 (the pK<sub>a</sub> of NH<sub>4</sub><sup>+</sup> ↔ NH<sub>3</sub> equilibrium), consistent with the formation of Na-carbonates.

#### 5.4.2. Relationship between pH and hydrothermal fluids

As mentioned above, some hydrothermal archaea can fix dissolved N<sub>2</sub> from hydrothermal fluids to produce NH<sub>4</sub><sup>+</sup>/NH<sub>3</sub> (Charlou et al., 2000; Mehta and Baross, 2006). In our case, it is unlikely that additional nitrogen was sourced from hydrothermal fluids, because Eu/Eu\* and TN are independent from each other (Fig. 14a; Fig. 14c). Furthermore, the strongly correlation between TN and TOC rules out exogenous nitrogen addition (Fig. 6a). Hence the nitrogen that is archived in these samples was primarily sourced from organic biomass that was buried during the time of deposition. In the CSR, both the hydrothermal fluid activity and δ<sup>15</sup>N values gradually decrease from P<sub>1f1</sub> to P<sub>1f3</sub> (Fig. 9), suggesting that hydrothermal fluids had a strong effect on the pH of the lake. In the CSR, the effect of the relatively deep hydrothermal fluids on δ<sup>15</sup>N values is reflected by the significant positive correlation between δ<sup>15</sup>N and Eu/Eu\* (R<sup>2</sup> = 0.55; Fig. 14b). This significantly positive correlation might be ascribed to the heat of hydrothermal fluids that would accelerate the rate of NH<sub>3</sub> volatilization and the increase in δ<sup>15</sup>N (Li et al., 2012; Deng et al., 2018). However, Na-carbonates are unstable at elevated temperatures (> 40°C) and plausible CO<sub>2</sub> levels (Jagniecki et al. 2015), and so the preservation of these minerals throughout our studied sections indicates that these hydrothermal fluids were probably not very hot by the time they entered the lake. The Eu anomaly, which requires high temperatures above 200°C, must have been generated deeper in the rock package. Another possible explanation is that hydrothermal fluids in CSR contributed directly to the increase of the pH through serpentinization of the deep-seated olivine-rich basalt (Renaut and Owen, 1988; Proskurowski et al., 2008; Zeng et al., 2002). Shibuya et al. (2013) showed that basalt can react with and absorb large amounts of CO<sub>2</sub>. As such, when ascending CO<sub>2</sub> encountered the early Carboniferous alkali olivine basalts in the Mahu Sag, it formed HCO<sub>3</sub><sup>-</sup> (Eq. 1; Pecoraino et al., 2015), and further hydrolysis of HCO<sub>3</sub><sup>-</sup> raised the pH of the hydrothermal fluids (Eq. 2; Pecoraino et al., 2015)

Basalt (plagioclase; olivine; pyroxene) + CO<sub>2</sub> + H<sub>2</sub>O →

Clay minerals + Ca<sup>2+</sup> + Mg<sup>2+</sup> + Na<sup>+</sup> + HCO<sub>3</sub><sup>-</sup> (Eq. 1)

HCO<sub>3</sub><sup>-</sup> + H<sub>2</sub>O → H<sub>2</sub>CO<sub>3</sub> + OH<sup>-</sup> (Eq. 2).

In addition, serpentinization of olivine often consumes H<sup>+</sup>, increasing the pH of hydrothermal fluids (Eqs 3–4; Proskurowski et al., 2008)

3FeMgSiO<sub>4</sub> (olivine) + 6H<sup>+</sup> → Fe<sub>3</sub>O<sub>4</sub> + 3Mg<sup>2+</sup> + 3SiO<sub>2</sub> + 2H<sub>2</sub>O + H<sub>2</sub> (Eq. 3)

H<sub>2</sub>O → H<sup>+</sup> + OH<sup>-</sup> (Eq. 4).

For example, in the Atlantic Lost City hydrothermal system, the pH of the hydrothermal fluid is as high as 9.0–9.8 due to olivine serpentinization (Proskurowski et al., 2008). Similar conditions have been reported from terrestrial springs associated with ophiolites (Szponar et al. 2013). Hence a strong influence of hydrothermal fluids on water pH is likely.

The decline in δ<sup>15</sup>N in the CSR from 22.71‰ in the lower P<sub>1f1</sub> to 19.06‰ in P<sub>1f2</sub> and 18.84‰ in the upper P<sub>1f3</sub> (Fig. 9) may indicate that the pH of this setting generally decreased up-section. At lower pH, a smaller fraction of NH<sub>4</sub><sup>+</sup> would have been converted to NH<sub>3</sub> with an overall less extreme isotopic effect.

In the TD, vertical  $\delta^{15}\text{N}$  variation is not as obvious as in the CSR, but the overall trend is similar.  $\delta^{15}\text{N}$  first increases and then decreases from P<sub>1f1</sub> to P<sub>1f2</sub> to P<sub>1f3</sub>, with average  $\delta^{15}\text{N}$  values of 20.7‰, 21.5‰, and 18.9‰, respectively.  $\delta^{15}\text{N}$  values of these samples show a weak positive correlation with Eu/Eu\* (Fig. 14d). The pH of the MTM, where  $\delta^{15}\text{N}$  values are less extreme, was perhaps lower due to freshwater influx, but the minimum  $\delta^{15}\text{N}$  value of 10.13‰ is similar to modern alkaline lakes (Fig. 13), suggesting that also this setting experienced alkaline pH conditions. Distal to the lake center the imprint of hydrothermal fluids is generally less evident (see above), but it is conceivable that alkalinity spread across the lake from central hydrothermal vents. Evaporation, which became more prominent late in the lake's history, as indicated by the salinity proxies, appears to have maintained high alkalinity as described from other alkaline lakes (Garrels and Mackenzie, 1967), but it was probably less effective in doing so compared to alkaline springs.

## 6. Conclusions

In summary (Fig. 15), our data suggest the following evolutionary trend for the alkaline Mahu Sag in terms of geochemistry:

(1) Our trace element data confirm that the lacustrine depositional setting of the Fengcheng Formation in the Mahu Sag, northwestern Junggar Basin, was affected by hydrothermal fluids, where the strongest influence from deep hydrothermal fluids was recorded in the center of the basin. The margins appear to have been affected by only shallow fluids – if at all. In general, hydrothermal fluid activity decreased over time.

(2) Z-values and  $\delta^{18}\text{O}_{\text{carb}}$  values record the water paleo-salinity better than TOC/TS and Y/Ho ratios, due to a variety of factors, including the involvement of hydrothermal fluids that perturbed trace element ratios. The salinity of the lake was highest in the center, possibly due to freshwater influx along the lake margins. The salinity gradually increased over time, possibly controlled by an increasingly arid climate.

(3)  $\delta^{15}\text{N}$  data robustly record lake paleo-pH. The pH of the lake interior was generally higher than along the margins, which may also be explained by freshwater influx, similar to the lower salinity in the marginal settings. The pH gradually decreased over time, counter to the salinity variation over time. This indicates the unsynchronized evolution of salinity and pH. Thus, pH was not driven exclusively by increasing evaporation. This observation contrasts with other settings where evaporation alone raises the pH (Garrels and Mackenzie 1967). In Mahu Sag, high-pH conditions were thus perhaps primarily driven by hydrothermal fluids.

Overall, our results thus provide new insights into an unusual alkaline lake setting in the Late Paleozoic. As noted above, alkaline lakes are known for displaying unusually high productivity, but the role of hydrothermal fluids in establishing such conditions, in addition to evapo-concentration (Garrels and Mackenzie 1967), was so far not well known. Our data begin to fill this gap and suggest that hydrothermal activity can create highly productive conditions conducive to the formation of alkaline conditions and associated petroleum source rocks.

## Acknowledgements

We thank the editor Dr Hailian Dong and three anonymous reviewers for their insightful comments and suggestions which greatly improved the manuscript. We thank technical staffs from the Research Institute of Experiment and Testing and Research Institute of Petroleum Exploration and Development of the PetroChina Xinjiang Oilfield Company for their cooperation during this study. This work was jointly funded by National Natural Science Foundation of China (Grant No. 41830425), National Science and Technology Major Project of China (Grant No. 2016ZX05003-005), and PetroChina Science and Technology Major Project (Grant No. 2017E-0401).

## References

- Ader, M., Thomazo, C., Sansjofre, P., Busigny, V., Papineau, D., Papineau, D., Cartigny, P., Halverson, G.P., 2016. Interpretation of the nitrogen isotopic composition of Precambrian sedimentary rocks: Assumptions and perspectives. *Chem. Geol.* 429, 93–110. <https://doi.org/10.1016/j.chemgeo.2016.02.010>.
- Arp, A. J., Childress, J.J., 1983. Sulfide Binding by the Blood of the Hydrothermal Vent Tube Worm *Riftia pachyptila*. *Science* 219, 295–297. <https://doi.org/10.1126/science.219.4582.295>.
- Arthur, M.A., Dean, W.E., Claypool, G.E., 1985. Anomalous  $^{13}\text{C}$  enrichment in modern marine organic carbon. *Nature* 315, 216–218. <https://doi.org/10.1038/315216a0>.
- Bau, M., Dulski, P., 1996. Distribution of yttrium and rare-earth elements in the Penge and Kuruman iron-formations, Transvaal Supergroup, South Africa. *Precambrian Res.* 79, 1–55. [https://doi.org/10.1016/0301-9268\(95\)00087-9](https://doi.org/10.1016/0301-9268(95)00087-9).
- Berner, R.A., Raiswell, R., 1984. C/S method for distinguishing freshwater from marine rocks. *Geology* 12, 365–368. [https://doi.org/10.1130/0091-7613\(1984\)12<365:CMFDFF>2.0.CO;2](https://doi.org/10.1130/0091-7613(1984)12<365:CMFDFF>2.0.CO;2).
- Cao, J., Lei, D.W., Li, Y.W., Tang, Y., Abulimit, Chang, Q.S., Wang, T.T., 2015. Ancient high-quality alkaline lacustrine source rocks discovered in the Lower Permian Fengcheng Formation, Junggar Basin. *Acta Petrolei Sinica* 36, 781–790. <https://doi.org/10.7623/syxb201507002>.
- Cao, J., Zhang, Y., Hu, W., Yao, S.P., Wang, X.L., Zhang, Y.Q., Tang, Y., 2005. The Permian hybrid petroleum system in the northwest margin of the Junggar Basin, northwest China. *Mar. Pet. Geol.* 22, 331–349. <https://doi.org/10.1016/j.marpetgeo.2005.01.005>.
- Carroll, A.R., 1998. Upper Permian lacustrine organic facies evolution, Southern Junggar Basin, NW China. *Org. Geochem.* 28, 649–667. [https://doi.org/10.1016/S0146-6380\(98\)00040-0](https://doi.org/10.1016/S0146-6380(98)00040-0).
- Chang, H.L., 2016. The Genesis of Exhalative Rocks of the Lower Permian Fengcheng Formation in Urho area, Northwestern Junggar. Chengdu University of technology, pp. 115. <http://cdmd.cnki.com.cn/Article/CDMD-10616-1016227280.htm>.
- Charlou, J.L., Donval, J.P., Douville, E., Jean-Baptiste, P., Radford-Knoery, J., Fouquet, Y., Dapigny, A., Stievenard, M., 2000. Compared geochemical signatures and the evolution of Menez Gwen ( $35^{\circ}50\text{N}$ ) and Lucky Strike ( $37^{\circ}17\text{N}$ ) hydrothermal fluids, south of the Azores Triple Junction on the Mid-Atlantic Ridge. *Chem. Geol.* 171, 49–75.

- [https://doi.org/10.1016/S0009-2541\(00\)00244-8](https://doi.org/10.1016/S0009-2541(00)00244-8).
- Couch, E.L., 1971. Calculation of paleosalinities from boron and clay mineral data. *AAPG Bull.* 55, 1829–1837. <https://doi.org/10.1306/819A3DAC-16C5-11D7-8645000102C1865D>.
- Degens, E.T., Williams, E.G., Keith, M.L., 1957. Environmental studies of carboniferous sediments part I: geochemical criteria for differentiating marine from fresh-water shales. *AAPG Bull.* 41, 2427–2455. <https://doi.org/10.1306/0BDA59A5-16BD-11D7-8645000102C1865D>
- Deng, Y., Li, Y., Li L., 2018. Experimental investigation of nitrogen isotopic effects associated with ammonia degassing at 0–70 °C. *Geochim. Cosmochim. Acta* 226, 182–191. <https://doi.org/10.1016/j.gca.2018.02.007>.
- Diamond, C.W., Planavsky, N.J., Wang, C., Lyons T.W., 2018. What the ~1.4 Ga Xiamaling Formation can and cannot tell us about the mid-Proterozoic ocean. *Geobiology* 16, 219–236. <https://doi.org/10.1111/gbi.12282>.
- Foster, G.L., Pogge von Strandmann, P.A.E., Rae, J.W.B., 2010. Boron and magnesium isotopic composition of seawater. *Geochem. Geophys. Geosy.* 11, 1525–2027. <https://doi.org/10.1029/2010GC003201>.
- Freitas, S.P., Clarke, L., Kennedy, H., Richardson, C.A., Abrantes, F.F., 2006. Environmental and biological controls on elemental (Mg/Ca, Sr/Ca and Mn/Ca) ratios in shells of the king scallop *Pecten maximus*. *Geochim. Cosmochim. Acta* 70, 5119–5133. <https://doi.org/10.1016/j.gca.2006.07.029>.
- Freudenthal, T., Wagner, T., Wenzhöfer, F., Zabel, M., Wefer, G., 2001. Early diagenesis of organic matter from sediments of the eastern subtropical Atlantic: evidence from stable nitrogen and carbon isotopes. *Geochim. Cosmochim. Acta* 65, 1795–1808. [https://doi.org/10.1016/S0016-7037\(01\)00554-3](https://doi.org/10.1016/S0016-7037(01)00554-3).
- Garrels, R.M., Mackenzie, F.T., 1967. Origin of the chemical composition of some springs and lakes. In: Stumm, W. (Ed.), *Equilibrium Concepts in Natural Water Systems*. American Chemical Society, Washington, DC, pp. 222–242. <https://doi.org/10.1021/ba-1967-0067.ch010>.
- Gislason, S.R., Eugster, P.E., 1987. Meteoric water-basalt interactions. I: A laboratory study. *Geochim. Cosmochim. Acta* 51, 2827–2840. [https://doi.org/10.1016/0016-7037\(87\)90161-X](https://doi.org/10.1016/0016-7037(87)90161-X).
- Godfrey, L.V., Glass, J.B., 2011. The Geochemical Record of the Ancient Nitrogen Cycle, Nitrogen Isotopes, and Metal Cofactors. *Methods Enzymol.* 486, 483–506. <https://doi.org/10.1016/B978-0-12-381294-0.00022-5>.
- Golan, R., Gavrieli, I., Ganor, J., Lazar, B., 2016. Controls on the pH of hyper-saline lakes – A lesson from the Dead Sea. *Earth Planet. Sci. Lett.* 434, 289–297. <https://doi.org/10.1016/j.epsl.2015.11.022>.
- Griffin, B.M., Schott, J., Schink, B., 2007. Nitrite, an electron donor for anoxygenic photosynthesis. *Science* 316, 1870–1870. <https://doi.org/10.1126/science.1139478>.
- Haendel, D., Muehle, K., Nitzsche, H.-M., Stiehl, G., Wand, U., 1986. Isotopic variations of the fixed nitrogen in metamorphic rocks. *Geochim. Cosmochim. Acta* 50, 749–758. [https://doi.org/10.1016/0016-7037\(86\)90351-0](https://doi.org/10.1016/0016-7037(86)90351-0)
- Hedenquist, J.W., Lowenstern, J.B., 1994. The role of magmas in the formation of

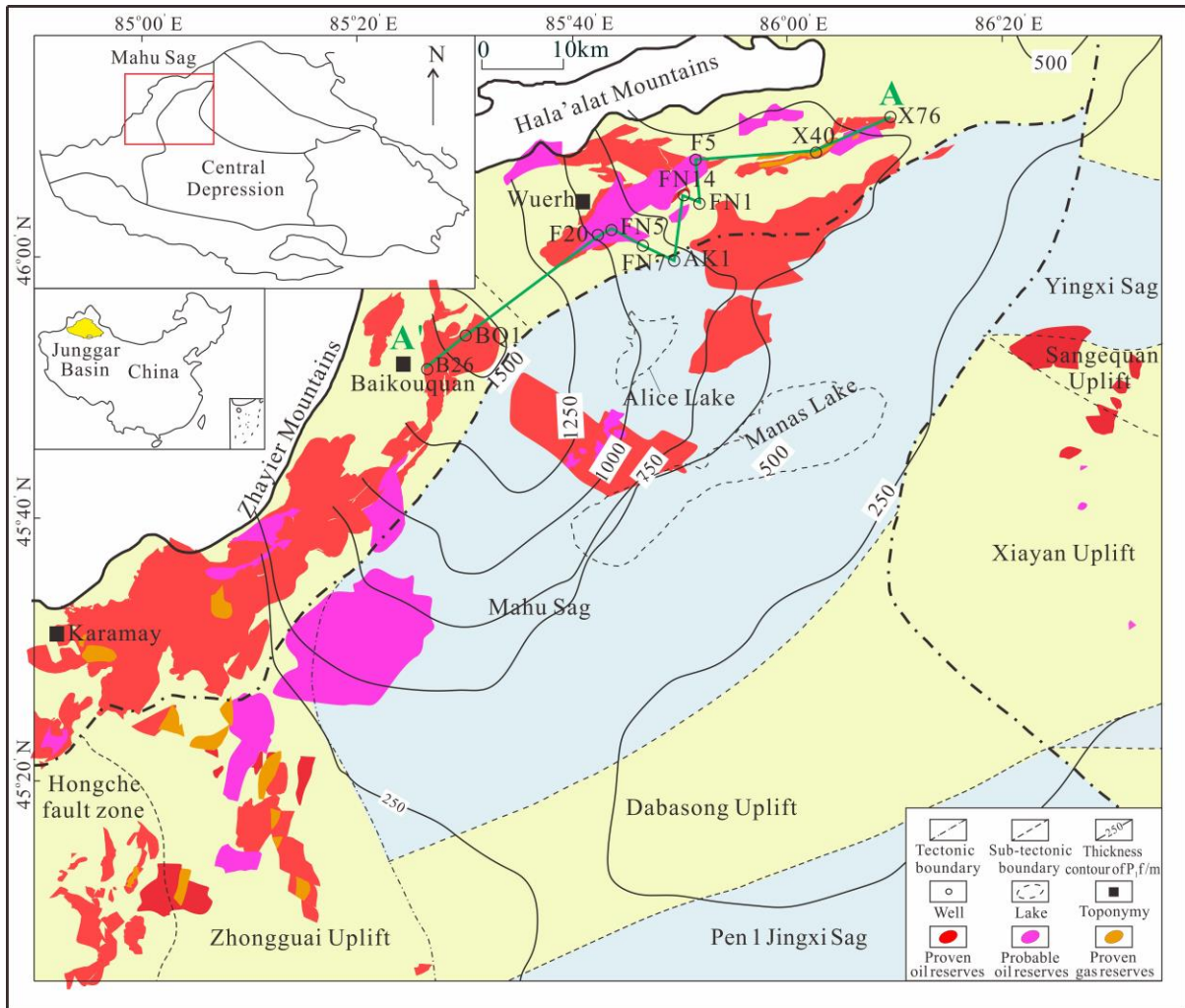
- hydrothermal ore deposits. *Nature* 370, 519–527. <https://doi.org/10.1038/370519a0>.
- Humphris, S.E., Bach, W., 2005. On the Sr isotope and REE compositions of anhydrites from the TAG seafloor hydrothermal system. *Geochim. Cosmochim. Acta* 69, 1511–1525. <https://doi.org/10.1038/370519a0>.
- Jagniecki, E.A., Lowenstein, T.K., Jenkins, D.M. and Demicco, R.V., 2015. Eocene atmospheric CO<sub>2</sub> from the nahcolite proxy. *Geology* 43, 1075–1078. <https://doi.org/10.1130/G36886.1>.
- Kaufman, A.J., Knoll, A.H., 1995. Neoproterozoic variations in the C-isotopic composition of seawater: stratigraphic and biogeochemical implications. *Precambrian Res.* 73, 27–49. [https://doi.org/10.1016/0301-9268\(94\)00070-8](https://doi.org/10.1016/0301-9268(94)00070-8)
- Keith, M.L., Weber, J.N., 1964. Carbon and oxygen isotopic composition of selected limestones and fossils. *Geochim. Cosmochim. Acta* 28, 1787–1816. [https://doi.org/10.1016/0016-7037\(64\)90022-5](https://doi.org/10.1016/0016-7037(64)90022-5).
- Kempe, S., Kazmierczak, J., 2003. Modern soda lakes – model environments for an early alkaline ocean. In: Mueller, T., Mueller, H. (Eds.), *Modelling in Natural Sciences*. Springer Verlag, Heidelberg, pp. 309–322. <https://doi.org/10.1007/978-3-662-05304-1>.
- Lawrence, M.G., Kamber, B.S., 2006. The behaviour of the rare earth elements during estuarine mixing-revisited. *Mar. Chem.* 100, 147–161. <https://doi.org/10.1016/j.marchem.2005.11.007>.
- Leboulanger, C., Agogu e, H., Bernard, C., Bouvy, M., Carr e, C., Cellamare, M., Duval, C., Fouilland, E., Got, P., Intertaglia, L., Lavergne, C., Floc’h, E.L., Roques, C., Sarazin, G., 2017. Microbial diversity and cyanobacterial production in Dziani Dzaha Crater Lake, a unique tropical Thalassohaline environment. *PLoS One* 12, 1–28 <https://doi.org/10.1371/journal.pone.0168879>.
- Li, L., Lollar, B.S., Li, H., Wortmann, U.G., Lacrampe-Couloume, G., 2012. Ammonium stability and nitrogen isotope fractionations for NH<sub>4</sub><sup>+</sup>–NH<sub>3(aq)</sub>–NH<sub>3(gas)</sub> systems at 20–70°C and pH of 2–13: Applications to habitability and nitrogen cycling in low-temperature hydrothermal systems. *Geochim. Cosmochim. Acta* 84, 280–296. <https://doi.org/10.1016/j.gca.2012.01.040>.
- Liu, W., Li, X., Zhang, L., An Z.S., Xu, L.M., 2009. Evaluation of oxygen isotopes in carbonate as an indicator of lake evolution in arid areas: The modern Qinghai Lake, Qinghai–Tibet Plateau. *Chem. Geol.* 268, 126–136. <https://doi.org/10.1016/j.chemgeo.2009.08.004>.
- McLauchlan, K.K., Williams, J.J., Craine, J.M., Jeffers, E.S., 2013. Changes in global nitrogen cycling during the Holocene epoch. *Nature* 495, 352–355. <https://doi.org/10.1038/nature11916>.
- Mehta, M.P., Baross, J.A., 2006. Nitrogen Fixation at 92°C by a Hydrothermal Vent Archaeon. *Science* 314, 1783–1786. <https://doi.org/10.1126/science.1134772>.
- M oller, P., Bau, M., 1993. Rare-earth patterns with positive cerium anomaly in alkaline waters from Lake Van, Turkey. *Earth Planet. Sci. Lett.* 117, 671–676. [https://doi.org/10.1016/0012-821X\(93\)90110-U](https://doi.org/10.1016/0012-821X(93)90110-U).
- Noll, P.D., Newsom, H E., Leeman, W.P., Ryann, J.G., 1996. The role of hydrothermal fluids in the production of subduction zone magmas: evidence from siderophile and chalcophile trace elements and boron. *Geochim. Cosmochim. Acta* 60, 587–611.

- [https://doi.org/10.1016/0016-7037\(95\)00405-X](https://doi.org/10.1016/0016-7037(95)00405-X).
- O'Neil, J.R., Epstein, S., 1966. Oxygen Isotope Fractionation in the System Dolomite-Calcite-Carbon Dioxide. *Science* 152, 198–201. <https://doi.org/10.1126/science.152.3724.997>.
- Pecoraino, G., D'Alessandro, W., Inguaggiato S., 2015. The Other Side of the Coin: Geochemistry of Alkaline Lakes in Volcanic Areas. In: Rouwet, D., Christenson, B., Tassi, F., Vandemeulebrouck, J. (Eds.), *Volcanic Lakes*. Springer, Berlin, Heidelberg, pp. 219–237. [https://doi.org/10.1007/978-3-642-36833-2\\_9](https://doi.org/10.1007/978-3-642-36833-2_9).
- Peters, K. E., C. C. Walters, Moldowan, J. M., 2005. *The biomarker guide*, 2nd ed.: Cambridge, United Kingdom, Cambridge University Press, 700 p.
- Polyak, L., Stanovoy, V., Lubinski, D.J., 2003. Stable isotopes in benthic foraminiferal calcite from a river-influenced Arctic marine environment, Kara and Pechora Seas. *Paleoceanography* 18, 1–17. <https://doi.org/10.1029/2001pa000752>
- Proskurowski, G., Lilley, M.D., Seewald, J.S., Früh-Green, G.L., Olson, E.J., Lupton, J.E., Sylva, S.P., Kelley, D.S., 2008. Abiogenic Hydrocarbon Production at Lost City Hydrothermal Field. *Science* 319, 604–607. <https://doi.org/10.1126/science.1151194>.
- Quan, T.M., Adigwe, E.N., Riedinger, N., Puckette, J., 2013. Evaluating nitrogen isotopes as proxies for depositional environmental conditions in shales: Comparing Caney and Woodford Shales in the Arkoma Basin, Oklahoma. *Chem. Geol.* 360–361, 231–240. <https://doi.org/10.1016/j.chemgeo.2013.10.017>.
- Rampelotto, P. H., 2013. Extremophiles and Extreme Environments. *Life* 3, 482–485. <https://doi.org/10.3390/life3030482>.
- Reghellin, D., Coxall, H.K., Dickens, G.R., Backman, J., 2015. Carbon and oxygen isotopes of bulk carbonate in sediment deposited beneath the eastern equatorial Pacific over the last 8 million years. *Paleoceanog. Paleoclimatol.* 30, 1261–1286. <https://doi.org/10.1002/2015PA002825>.
- Renaut, R.W., Owen, R.B., 1988. Opaline cherts associated with sublacustrine hydrothermal springs at Lake Bogoria, Kenya Rift Valley. *Geology* 16, 699–702. [https://doi.org/10.1130/0091-7613\(1988\)016<0699:OCAWSH>2.3.CO;2](https://doi.org/10.1130/0091-7613(1988)016<0699:OCAWSH>2.3.CO;2).
- Roscher, M., Schneider, J.W., 2006. Permo-Carboniferous climate: Early Pennsylvanian to Late Permian climate development of central Europe in a regional and global context. *Geo. Soc. London Special Pub.* 265, 95–136. <https://doi.org/10.1144/GSL.SP.2006.265.01.05>.
- Rothschild, L.J., Mancinelli, R.L., 2001. Life in extreme environments. *Nature* 409, 1092–1101. <https://doi.org/10.1038/35059215>.
- Shibuya, T., Yoshizaki, M., Masaki, Y., Suzuki, K., Takai, K., Russell, M., 2013. Reactions between basalt and CO<sub>2</sub>-rich seawater at 250 and 350°C, 500bars: Implications for the CO<sub>2</sub> sequestration into the modern oceanic crust and the composition of hydrothermal vent fluid in the CO<sub>2</sub>-rich early ocean. *Chem. Geol.* 359, 1–9. <https://doi.org/10.1016/j.chemgeo.2013.08.044>.
- Sigman, D.M., Karsh, K.L., Casciotti, K.L., 2009. Nitrogen isotopes in the ocean. In: Steele, J.H., Turekian, K.K., Thorpe S.A. (Eds.), *Encyclopedia of Ocean Sciences*, 2nd ed. Academic Press, London, pp. 40–54. <https://doi.org/10.1016/B978-012374473-9.00632-9>.

- Stam, M.C., Mason, P.R.D., Céline, Pallud, C., Cappellen, P.V., 2010. Sulfate reducing activity and sulfur isotope fractionation by natural microbial communities in sediments of a hypersaline soda lake (Mono Lake, California). *Chem. Geol.* 278, 23–30. <https://doi.org/10.1016/j.chemgeo.2010.08.006>.
- Stüeken, E.E., Buick, R., 2017. Environmental control on microbial diversification and methane production in the Mesoarchean. *Precambrian Res.* 304, 64–72. <https://doi.org/10.1016/j.precamres.2017.11.003>.
- Stüeken, E.E., Buick, R., Schauer, A.J., 2015. Nitrogen isotope evidence for alkaline lakes on late Archean continents. *Earth Planet. Sci. Lett.* 411, 1–10. <https://doi.org/10.1016/j.epsl.2014.11.037>.
- Stüeken, E.E., Kipp, M.A., Koehler, M.C., Buick, R., 2016. The evolution of Earth's biogeochemical nitrogen cycle. *Earth-Sci. Rev.* 160, 220–239. <https://doi.org/10.1016/j.earscirev.2016.07.007>.
- Stüeken, E.E., Martinez, A., Love, G., Olsen, P.E., Bates, S., Lyons, T.W., 2019. Effects of pH on redox proxies in a Jurassic rift lake: Implications for interpreting environmental records in deep time. *Geochim. Cosmochim. Acta* 252, 240–267. <https://doi.org/10.1016/j.gca.2019.03.014>.
- Sugitani, K., Yamashita, F., Nagaoka, T., Nagaoka, T., Yamamoto, K., Minami, M., Minami, K., Suzuki, K., 2006. Geochemistry and sedimentary petrology of Archean clastic sedimentary rocks at Mt. Goldsworthy, Pilbara Craton, Western Australia: Evidence for the early evolution of continental crust and hydrothermal alteration. *Precambrian Res.* 147(1), 124–147. <https://doi.org/10.1016/j.precamres.2006.02.006>.
- Szponar, N., Brazelton, W.J., Schrenk, M.O., Bower, D.M., Steele, A., Morrill, P.L., 2013. Geochemistry of a continental site of serpentinization, the Tablelands Ophiolite, Gros Morne National Park. *Icarus* 224, 286–296. <https://doi.org/10.1016/j.icarus.2012.07.004>.
- Talbot, M.R., Johannessen, T., 1992. A high resolution palaeoclimatic record for the last 27,500 years in tropical west Africa from the carbon and nitrogen isotopic composition of lacustrine organic matter. *Earth Planet. Sci. Lett.* 110, 23–37. [https://doi.org/10.1016/0012-821x\(92\)90036-u](https://doi.org/10.1016/0012-821x(92)90036-u).
- Tesdal, J., Galbraith, E.D., Kienast, M., 2013. Nitrogen isotopes in bulk marine sediment: linking seafloor observations with subseafloor records. *Biogeosciences* 10, 101–118. <https://doi.org/10.5194/bg-10-101-2013>.
- Vengosh, A., Kolodny, Y., Starinsky, A., Chivas, A.R., McCulloch, M.T., 1991. Coprecipitation and isotopic fractionation of boron in modern biogenic carbonates. *Geochim. Cosmochim. Acta* 55, 2901–2910. [https://doi.org/10.1016/0016-7037\(91\)90455-E](https://doi.org/10.1016/0016-7037(91)90455-E).
- Wei, W., Algeo, T. J., Lu, Y., Lu, Y. C., Liu, H. M., Zhang, S. P., Peng, L., Zhang, J. Y., Chen, L., 2018. Identifying marine incursions into the Paleogene Bohai Bay Basin lake system in northeastern China. *Int. J. Coal Geol.* 2018, 1–17. <https://doi.org/10.1016/j.coal.2018.10.001>.
- Wei, W., Algeo, T.J., 2019. Elemental proxies for paleosalinity analysis of ancient shales and mudrocks. *Geochim. Cosmochim. Acta*. In press. doi: 10.1016/j.gca.2019.06.034.
- Wunder, B., Stefanski, J., Wirth, R., Gottschalk, M., 2013. Al-B substitution in the system albite (NaAlSi<sub>3</sub>O<sub>8</sub>)–reedmergnerite (NaBSi<sub>3</sub>O<sub>8</sub>). *Eur. J. Mineral.* 25, 499–508.

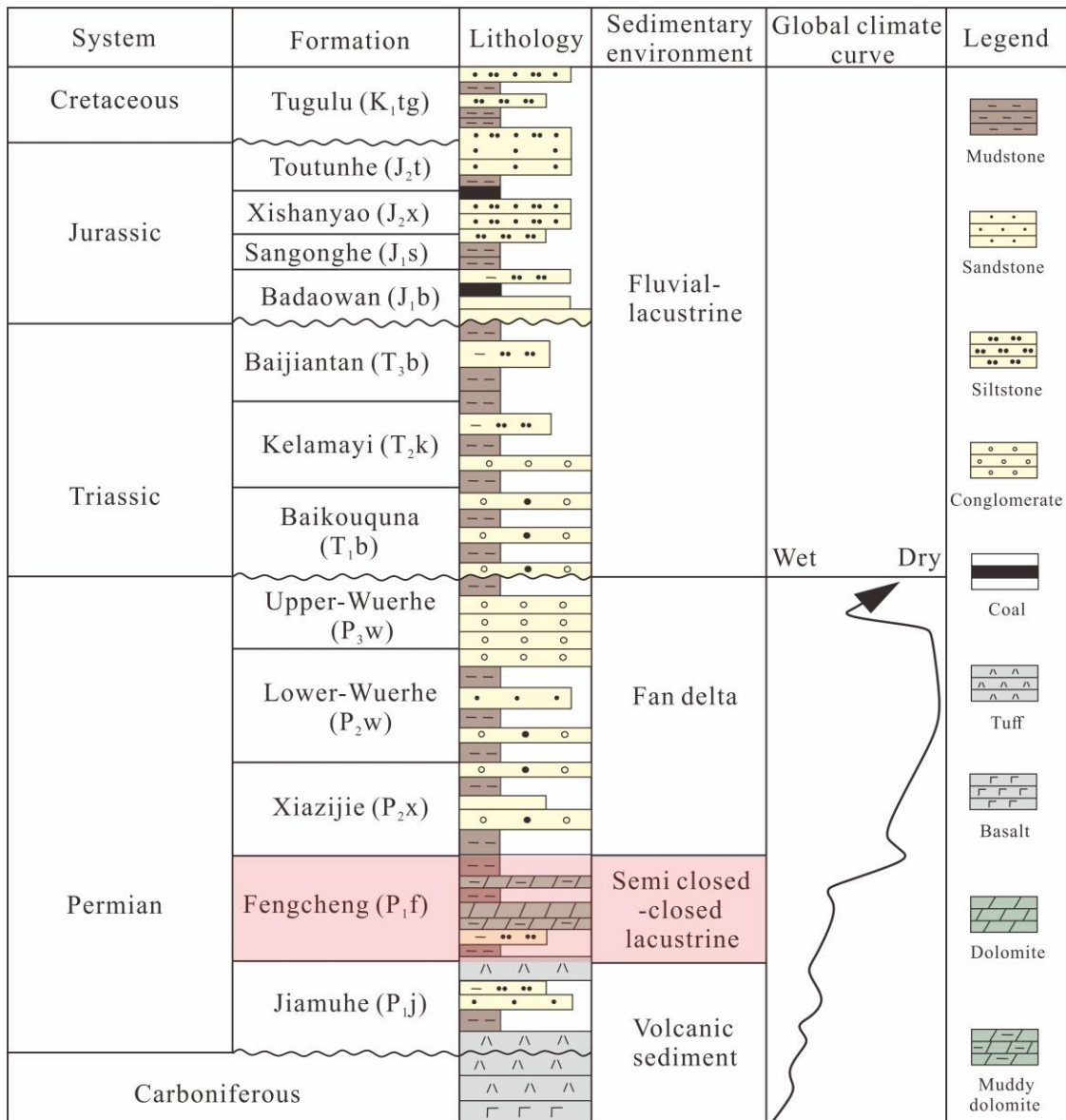
- <https://doi.org/10.1127/0935-1221/2013/0025-2286>.
- Yao, W., Millero, F.J., 1996. Oxidation of hydrogen sulfide by hydrous Fe(III) oxides in seawater. *Mar. Chem.* 52 (1), 1–16. [https://doi.org/10.1016/0304-4203\(95\)00072-0](https://doi.org/10.1016/0304-4203(95)00072-0).
- Yu, K.H., Cao, Y.C., Qiu, L.W., Sun, P.P., Jia, X.Y., Wan, M., 2018. Geochemical characteristics and origin of sodium carbonates in a closed alkaline basin: The Lower Permian Fengcheng Formation in the Mahu Sag, northwestern Junggar Basin, China. *Palaeogeogr. Palaeoclimatol. Palaeoecol.* 511, 506–531. <https://doi.org/10.1016/j.palaeo.2018.09.015>.
- Zeng, G.C., Wang, F.Z., Zheng, J.P., Cheng, Z.M., 2002. Study of Pyroxene in Junggar Basin Basement Volcanic Rock and Its Indicator to Basin Basement Characteristics. *Earth Science-Journal of China University of Geosciences* 27, 13–18. <https://doi.org/10.3321/j.issn:1000-2383.2002.01.003>.
- Zhang, L.C., Wan, B., Jiao, X.J., Zhang, R., 2006. Characteristics and geological significance of adakitic rocks in copper-bearing porphyry in Baogutu, western Junggar. *Geology in China* 33, 626–631. <https://doi.org/10.3969/j.issn.1000-3657.2006.03.020>.
- Zheng, Y.F., Hoefs, J., 1993. Carbon and oxygen isotopic covariations in hydrothermal calcites. *Mineral. Deposita* 28, 79–89. <https://doi.org/10.1007/BF00196332>.

## Figure 1



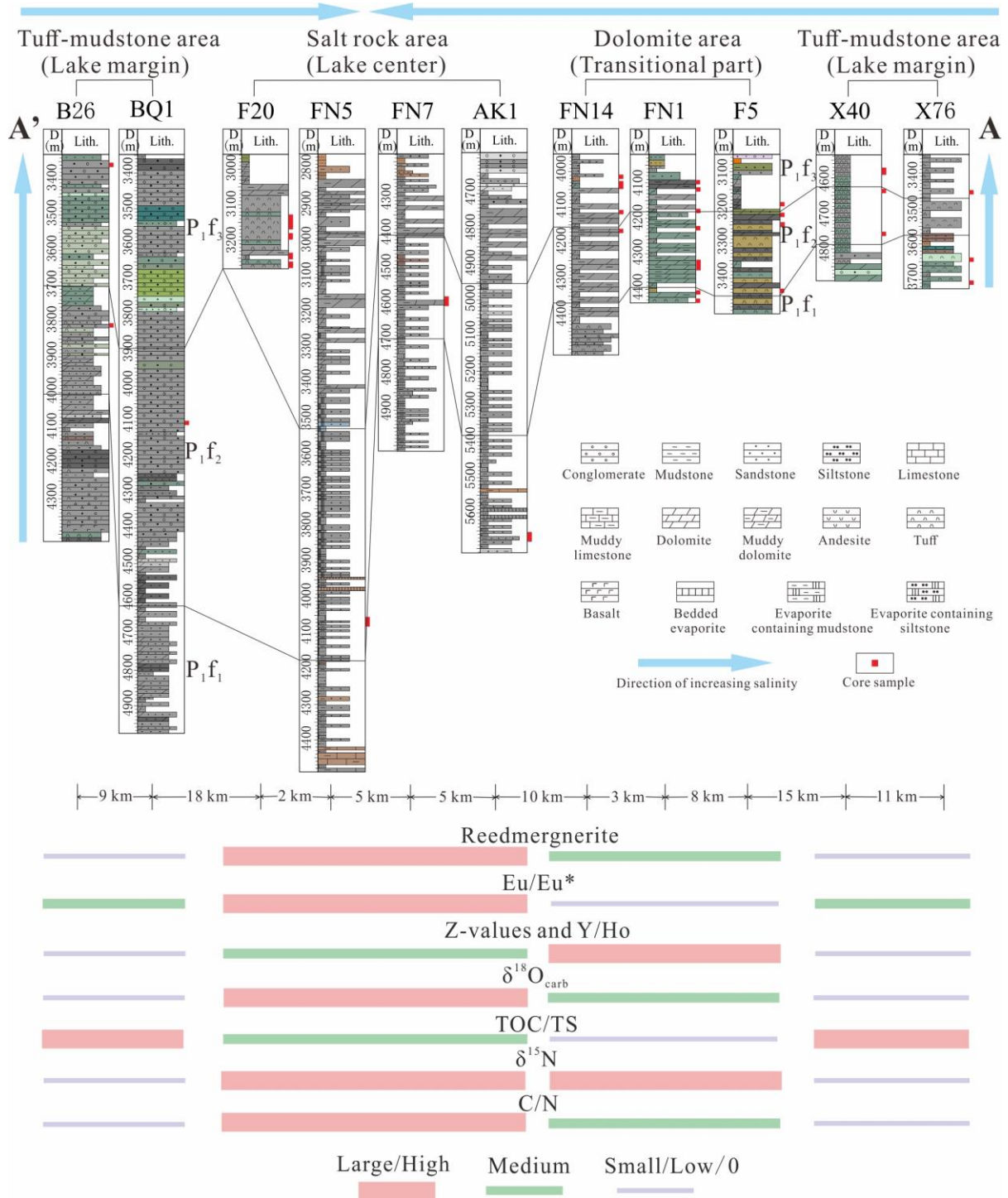
**Fig. 1.** Structural setting and distribution of petroleum resources in the Mahu Sag, Junggar Basin. Localities of cores investigated in this study are marked (F20, FN5, FN7, and AK1 in the CSR; F5, FN1, and FN14 in the TD; X40, X76, BQ1, and B26 from MTM). The green line from A' to A corresponds to the basinal section shown in Figure 3. The grey and light yellow areas refer to sags and uplifts.

**Figure 2**



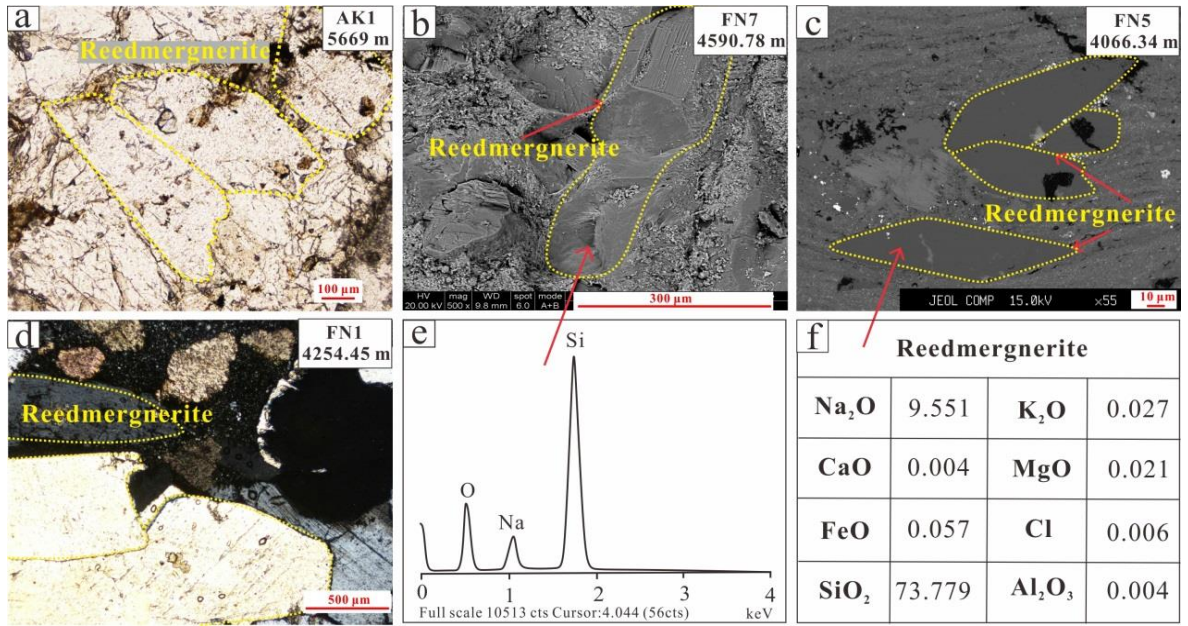
**Fig. 2.** Stratigraphy of the western Junggar Basin. The global climate curve is taken from Roscher and Schneider, 2006. Our study site is marked in light red and was deposited during a time of progressive warming and drying.

**Figure 3**



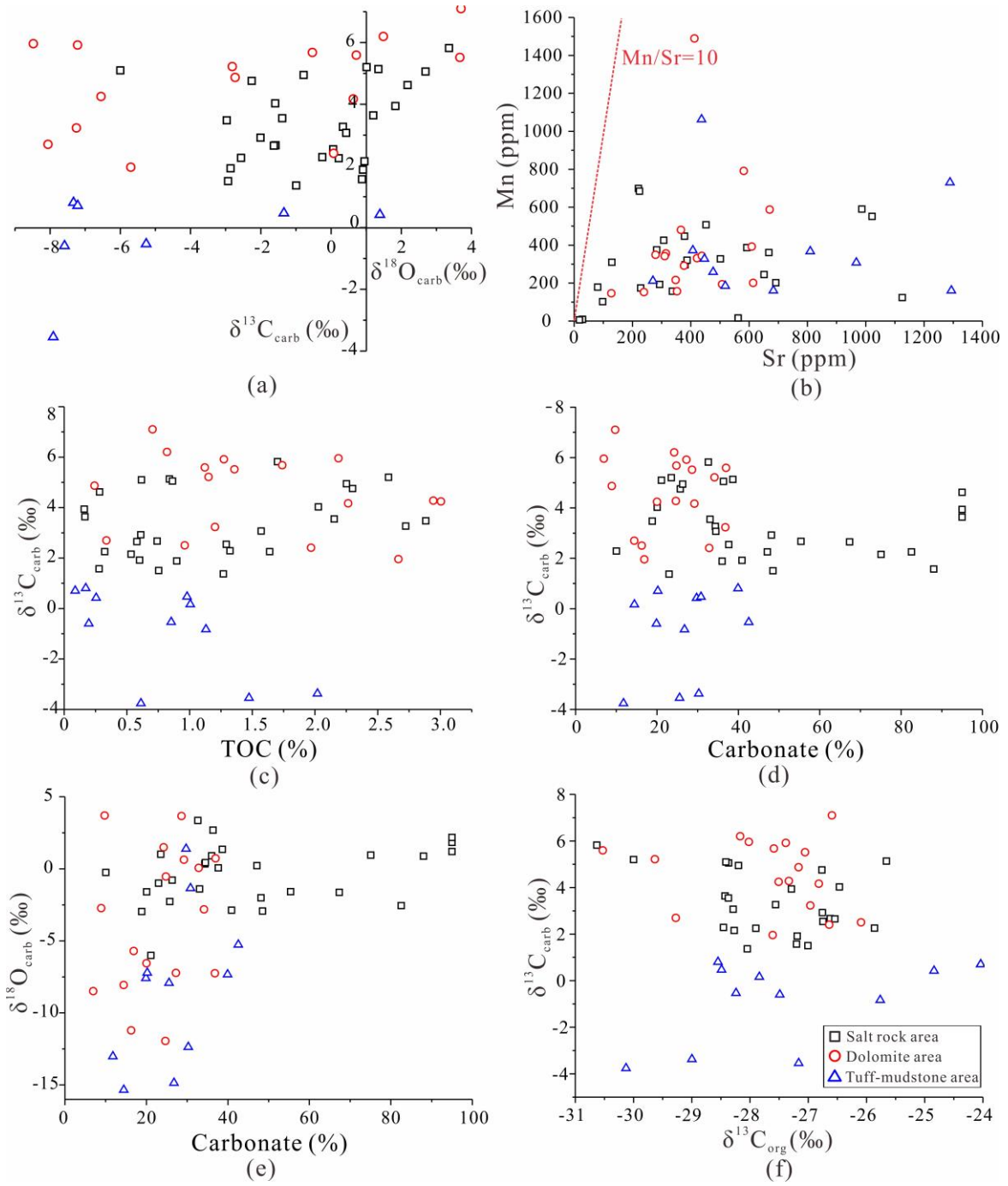
**Fig. 3.** Core stratigraphy of the Fengcheng Formation in the Mahu Sag. Salinity increases from the lake margins towards the center and up section (blue arrows).

Figure 4



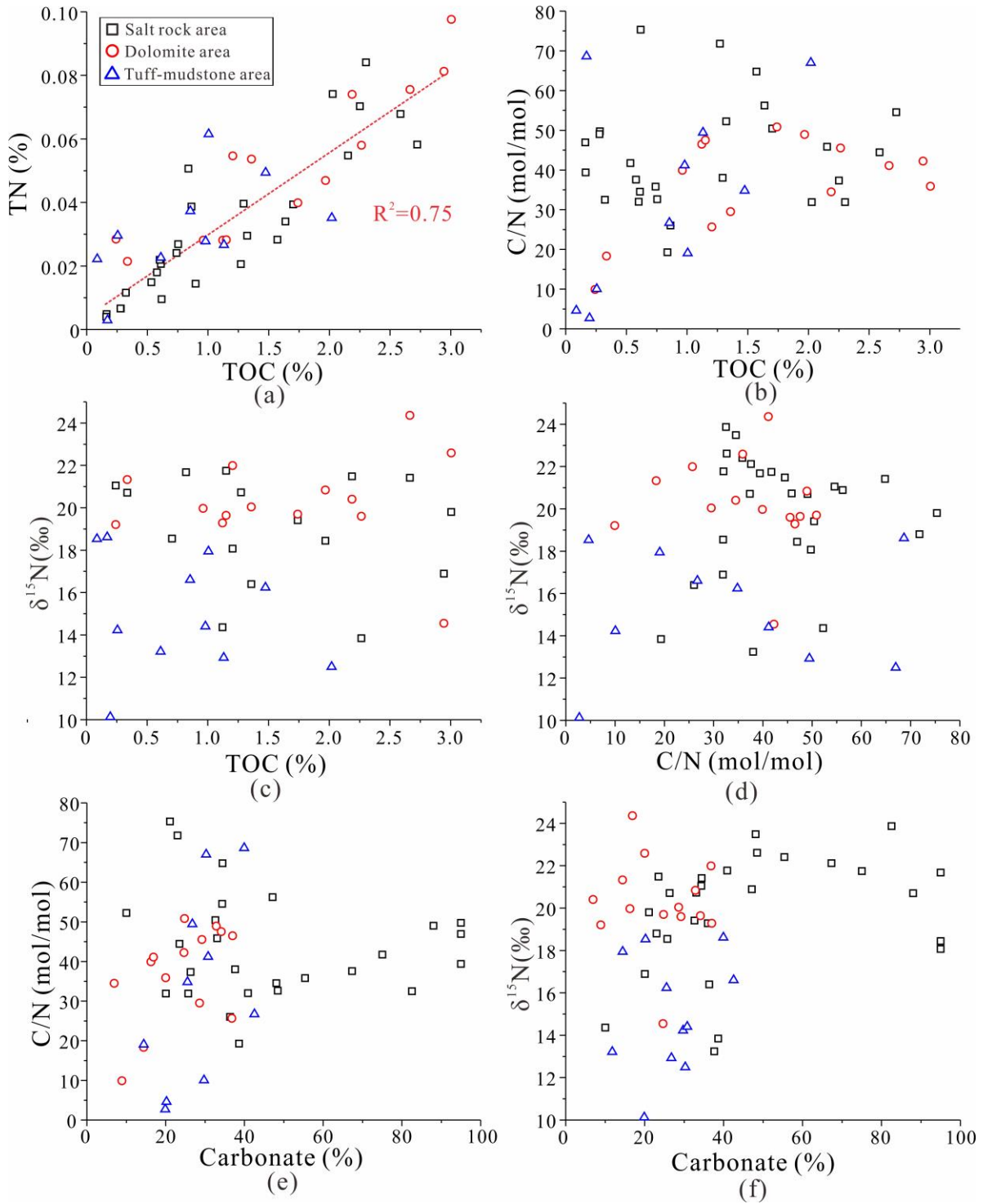
**Fig. 4.** Reedmergnerite in the Fengcheng Formation. (a) photomicrograph under plane-polarized light; (b) SEM image; (c) back-scattered electron image; (d) photomicrograph under cross-polarized light; (e) EDS spectrum; (f) mineral chemistry.

**Figure 5**



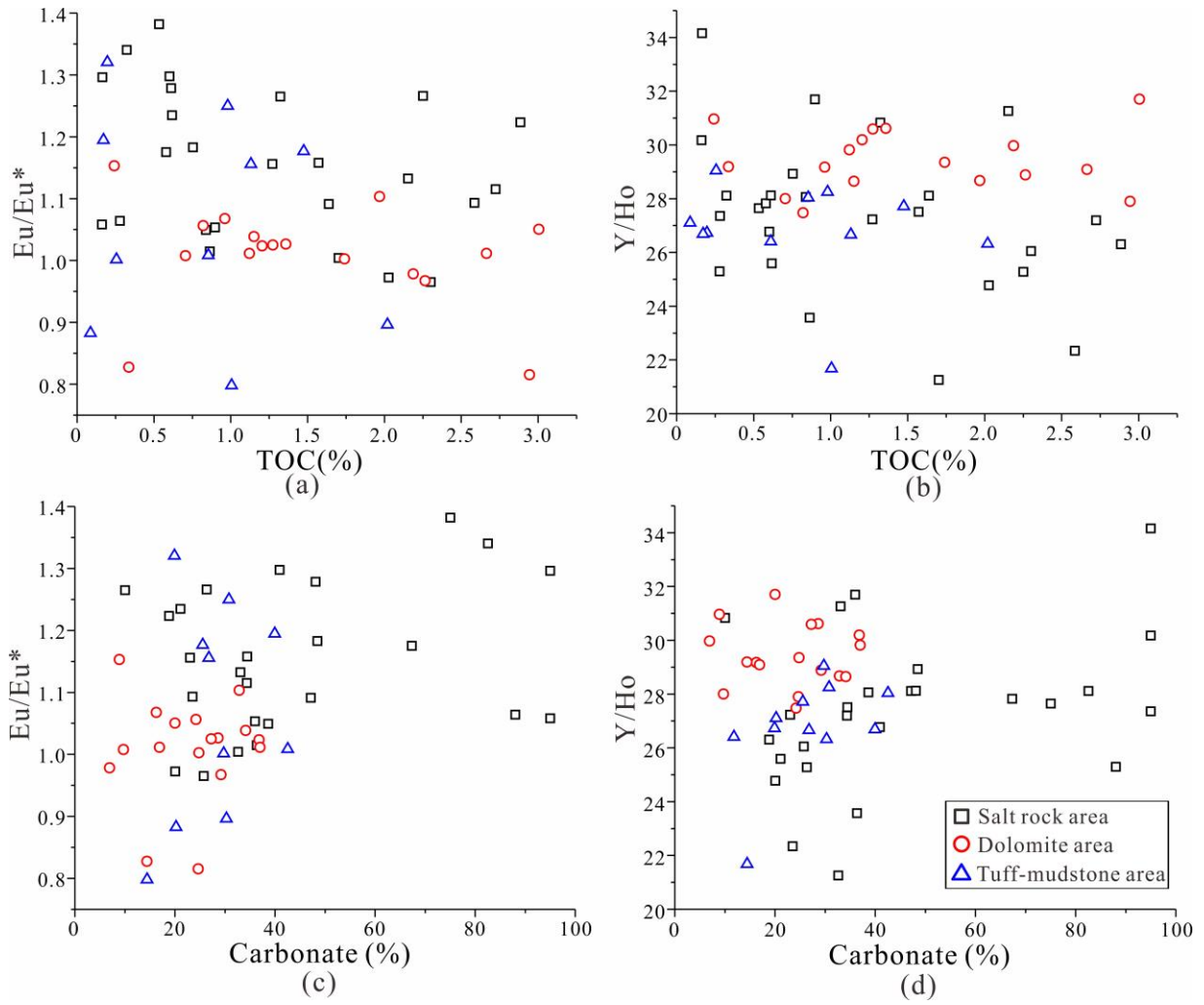
**Fig. 5.** Carbon-oxygen scattering plots and Mn contents versus Sr contents in the Fengcheng Formation in the Mahu Sag. (a)  $\delta^{13}\text{C}_{\text{carb}}$  versus  $\delta^{18}\text{O}_{\text{carb}}$ ; (b) Mn contents vs Sr contents; (c)  $\delta^{13}\text{C}_{\text{carb}}$  versus TOC; (d)  $\delta^{13}\text{C}_{\text{carb}}$  versus carbonate contents; (e)  $\delta^{18}\text{O}_{\text{carb}}$  versus carbonate contents; (f)  $\delta^{18}\text{O}_{\text{carb}}$  versus  $\delta^{13}\text{C}_{\text{org}}$ .

Figure 6



**Fig. 6.** Carbon-nitrogen scattering plots in the Fengcheng Formation in the Mahu Sag. (a) TN versus TOC; (b) TOC/TN vs TOC; (c)  $\delta^{15}\text{N}$  versus TOC; (d)  $\delta^{15}\text{N}$  versus TOC/TN; (e) TOC/TN versus carbonate contents; (f)  $\delta^{15}\text{N}$  versus carbonate contents.

**Figure 7**



**Fig. 7.** Effects of diagenesis on  $Eu/Eu^*$  and  $Y/Ho$  in the Fengcheng Formation in the Mahu Sag. (a)  $Eu/Eu^*$  versus TOC; (b)  $Y/Ho$  versus TOC; (c)  $Eu/Eu^*$  versus carbonate contents; (d)  $Y/Ho$  versus carbonate contents.

Figure 8

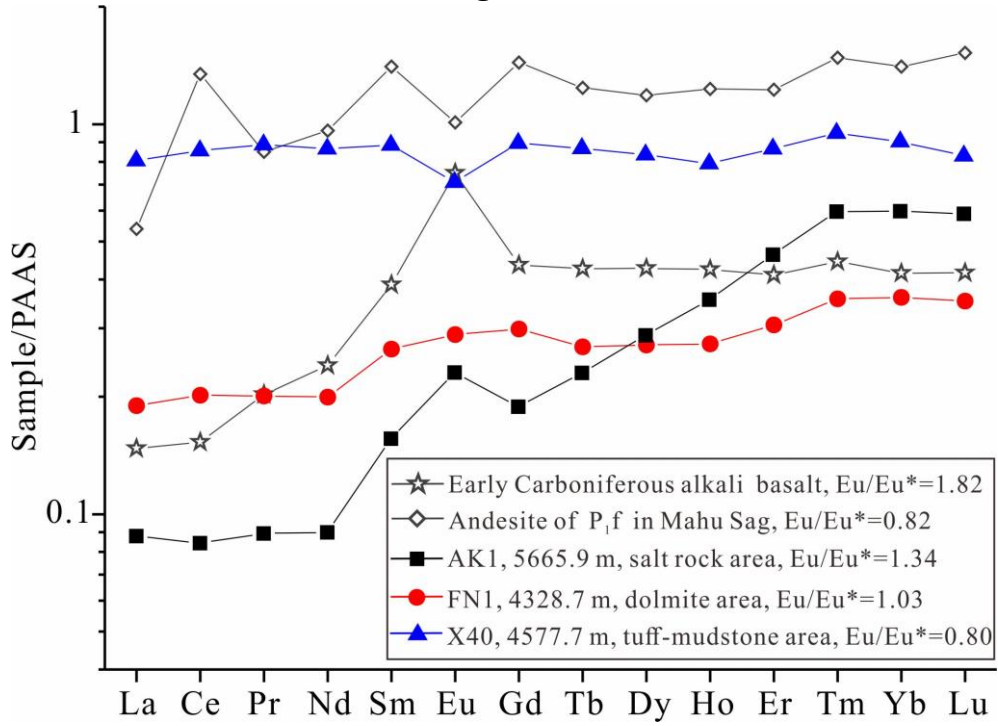
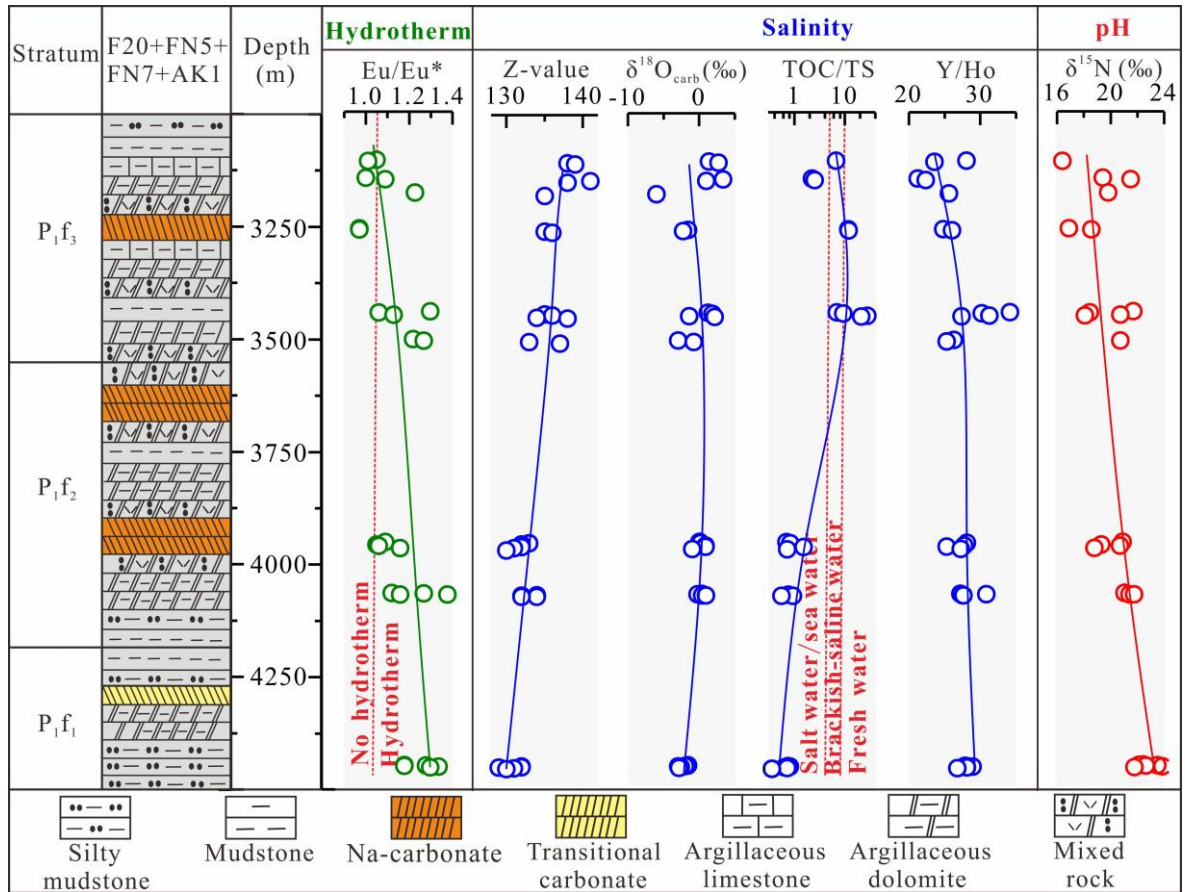


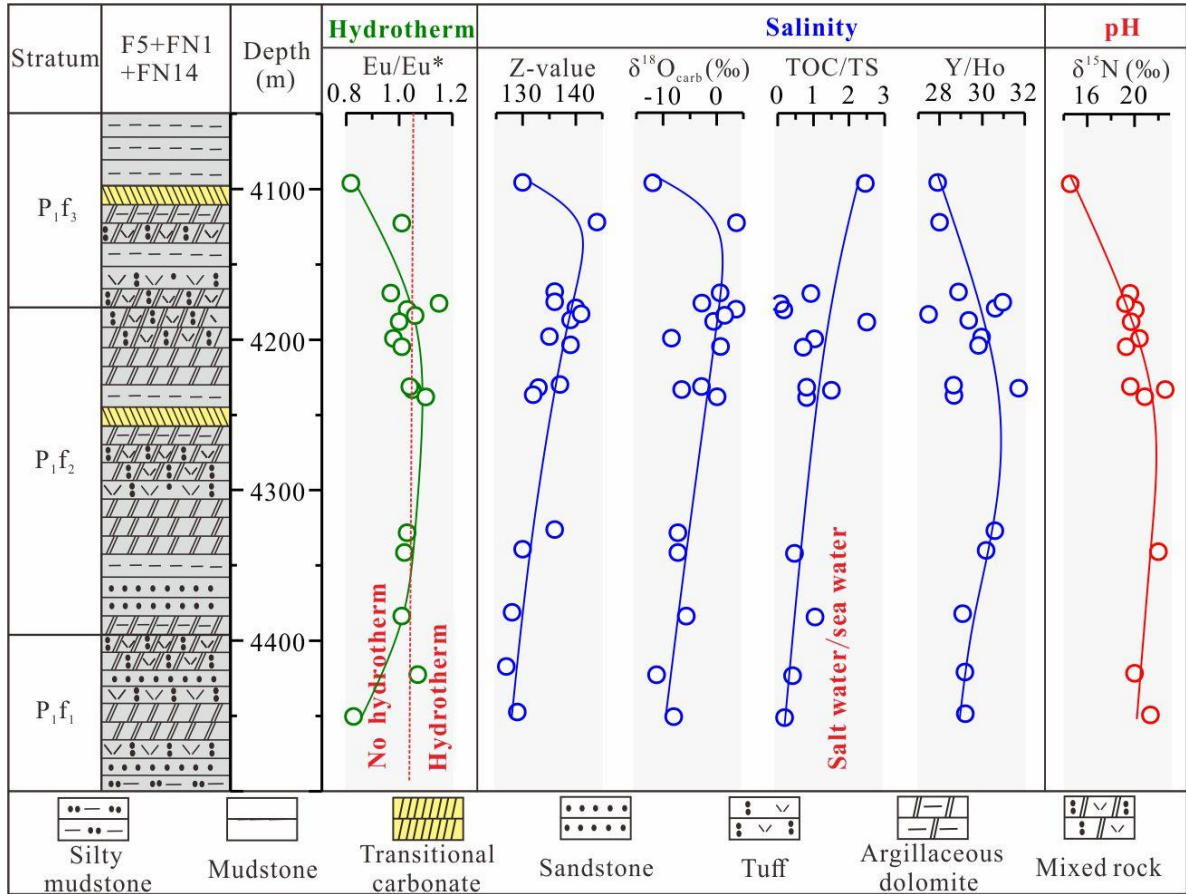
Fig. 8. REE data for the Fengcheng Formation in the Mahu Sag normalized to PAAS (post-Archean Australian Shale).

Figure 9



**Fig. 9.** Z-values,  $\delta^{18}O_{carb}$ , TOC/TS, Y/Ho,  $\delta^{15}N$ , and Eu/Eu\* data plotted versus depth for the CSR of the Fengcheng Formation in the Mahu Sag. The depths of samples from F20, FN7 and AK1 are converted into equivalent depths of FN5 based on strata data.

**Figure 10**



**Fig. 10.** Z-values,  $\delta^{18}O_{carb}$ , TOC/TS, Y/Ho,  $\delta^{15}N$ , and Eu/Eu\* data plotted versus depth for the transitional dolomite area of the Fengcheng Formation in the Mahu Sag. The depths of samples from F5 and FN14 are converted into equivalent depths of FN1 based on strata data.

**Figure 11**

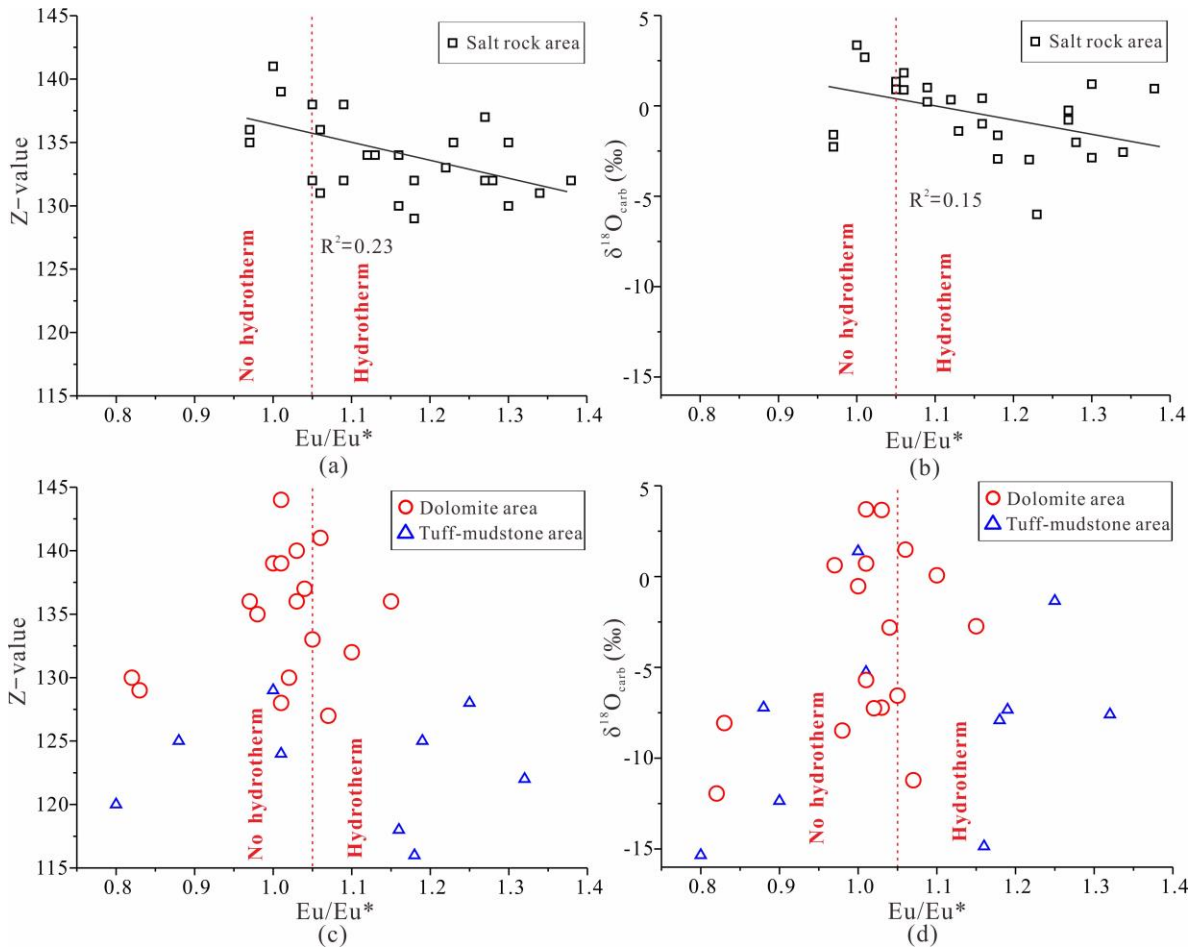


**Fig. 11.** Effects of hydrothermal fluids on Z-values and  $\delta^{18}\text{O}_{\text{carb}}$  values in the Fengcheng Formation in the Mahu Sag. (a) Z-values in the CSR; (b)  $\delta^{18}\text{O}_{\text{carb}}$  values in the CSR; (c) Z-values in the TD and MTM; (d)  $\delta^{18}\text{O}_{\text{carb}}$  values in the TD and MTM.

**Figure 12**

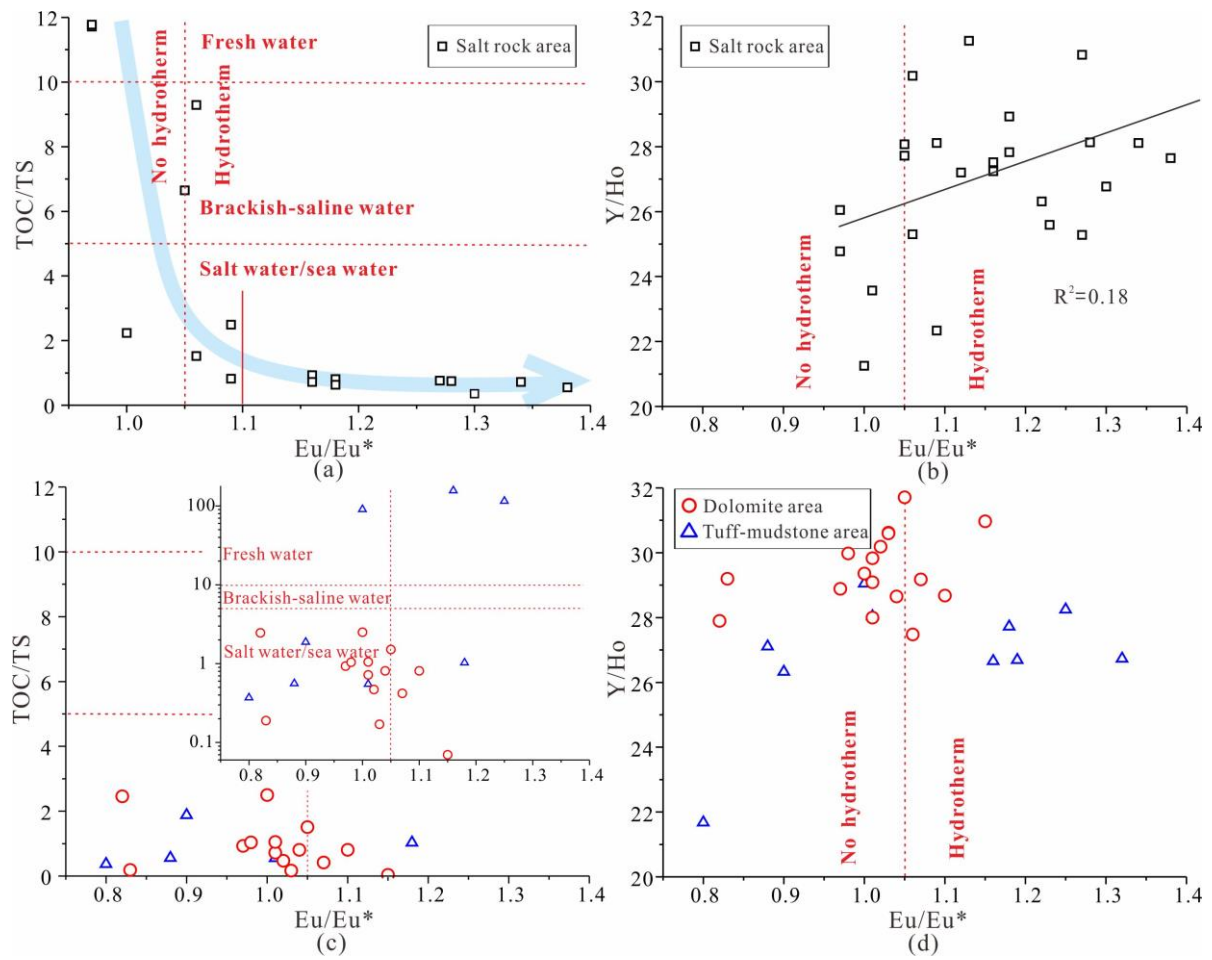


**Fig. 12.** Effects of hydrothermal fluids on TOC/TS and Y/Ho ratios in the Fengcheng Formation in the Mahu Sag. (a) TOC/TS in the CSR (b) Y/Ho in the CSR; (c) TOC/TS in the TD and MTM; (d) Y/Ho in the TD and MTM.

**Figure 13**

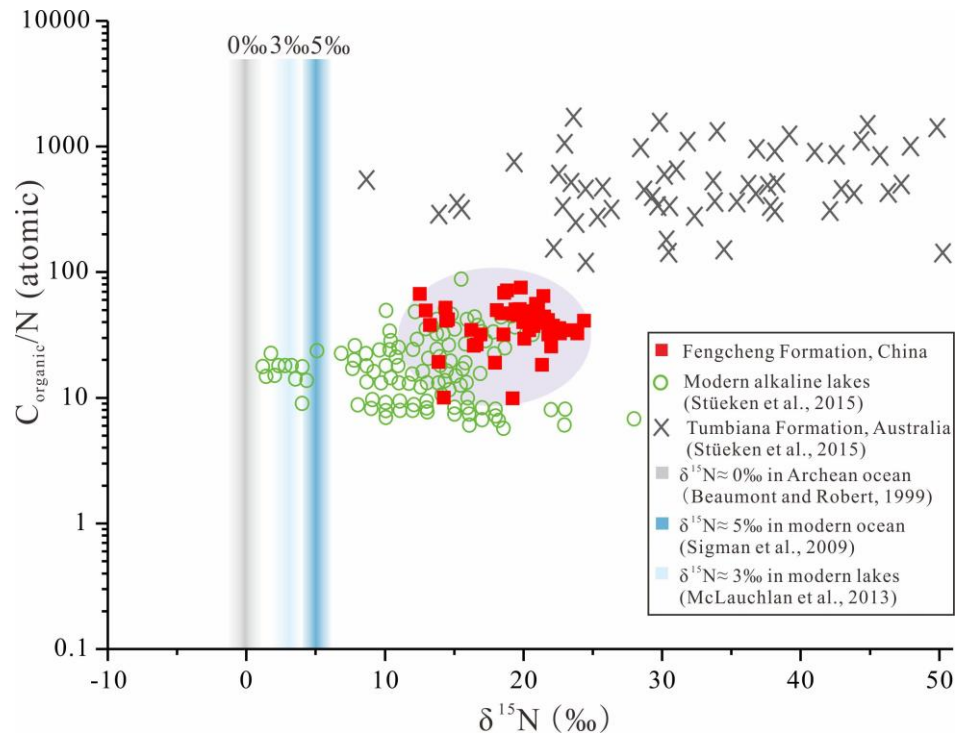


**Fig. 13.**  $C_{\text{org}}/N$  versus  $\delta^{15}N$  in the Fengcheng Formation in the Mahu Sag.

Figure 14

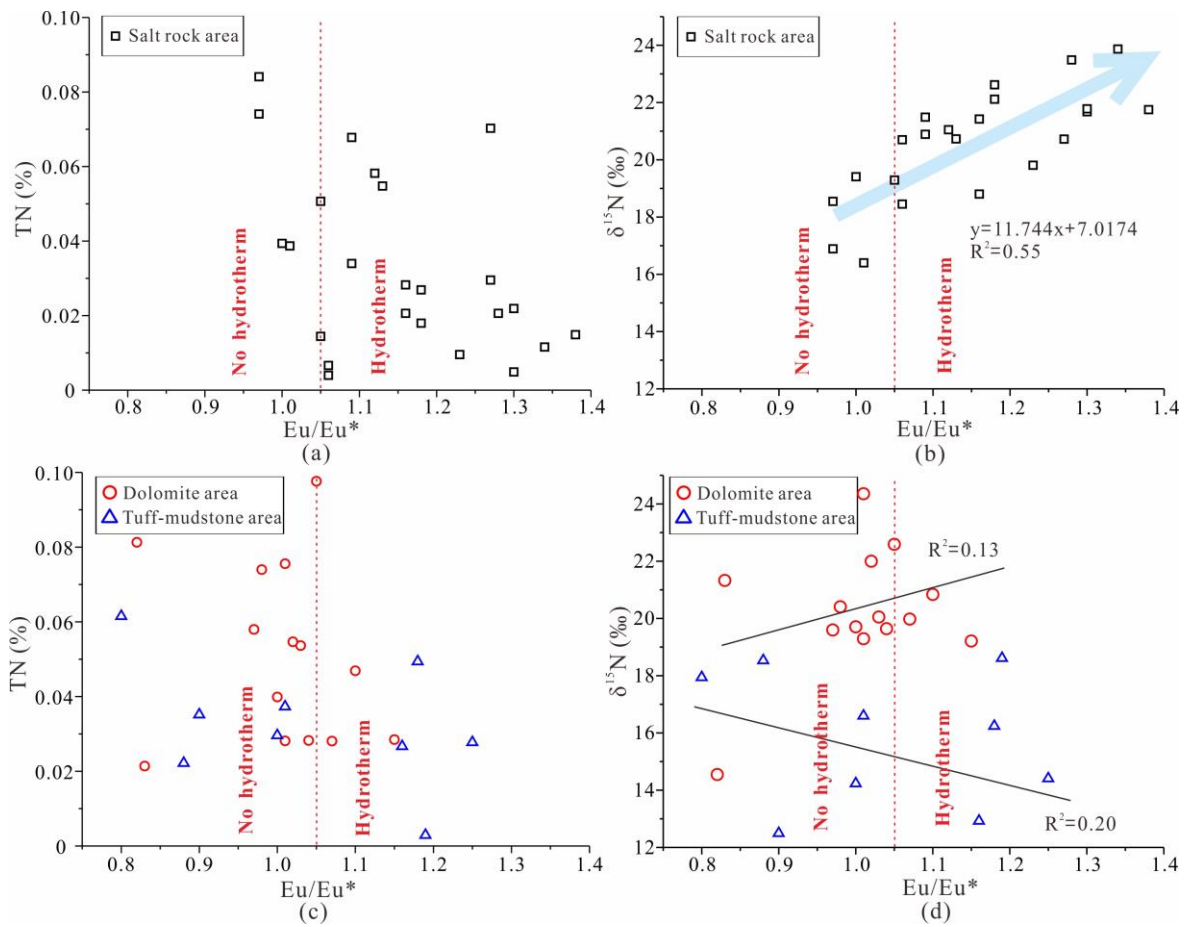


**Fig. 14.** Effects of hydrothermal fluids on pH in the Fengcheng Formation in the Mahu Sag. (a) TN in the CSR; (b) TN in the TD and MTM; (c)  $\delta^{15}\text{N}$  in the CSR (d)  $\delta^{15}\text{N}$  in the TD and MTM.

Figure 15

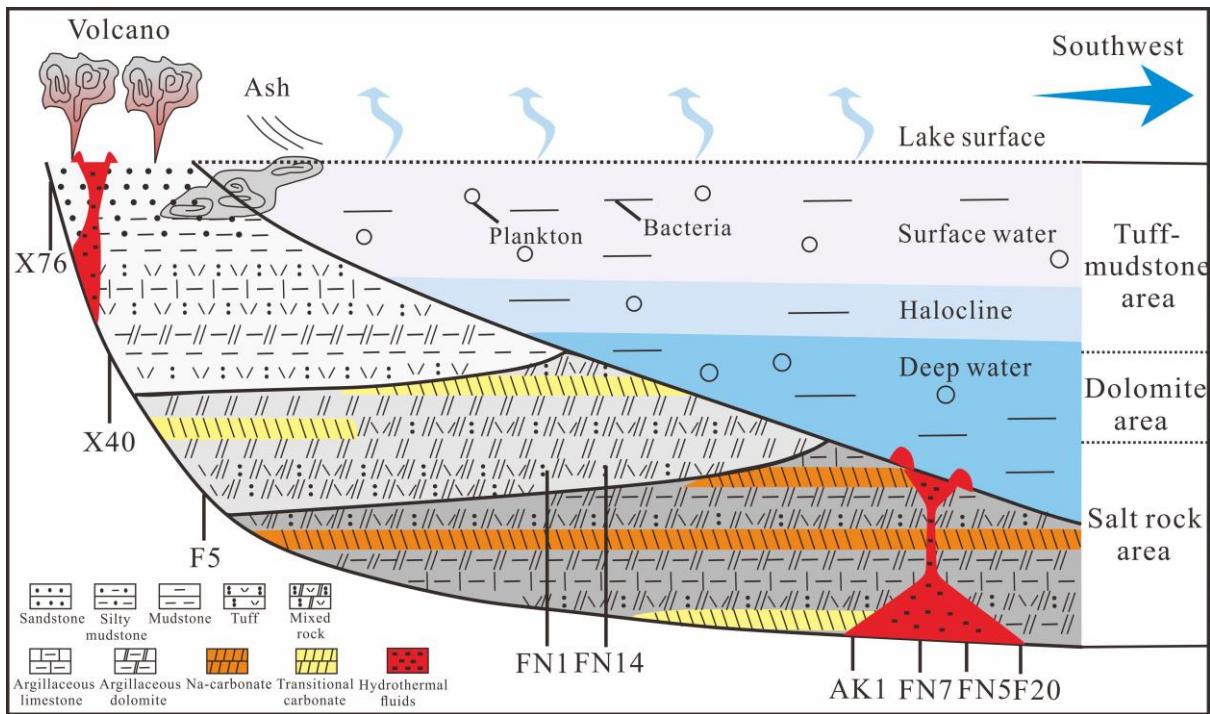


Fig. 15. Model of the development of the alkaline lake in the Mahu Sag.

**Table 1:** Eu/Eu\* values of the Fengcheng Formation in the Mahu Sag. A = average, N = number of samples, SD = standard deviation.

Area Proxies	CSR (Wells F20, FN5, FN7, AK1)			TD (Wells F5, FN1, FN14)	MTM (Wells X40, X76, BQ1, B26)
<b>Eu/Eu*</b>	0.97–1.64, A = 1.17, N = 28, SD = 0.15			0.82–1.15, A = 1.01, N = 17, SD = 0.08	0.8–1.32, A = 1.07, N = 11, SD = 0.17
	P <sub>1f1</sub> 1.18–1.34, A = 1.25, N = 6, SD = 0.07	P <sub>1f2</sub> 1.05–1.38, A = 1.16, N = 9, SD = 0.10	P <sub>1f3</sub> 0.97–1.64, A = 1.15, N = 13, SD = 0.18		

**Table 2:** Z-values,  $\delta^{18}\text{O}_{\text{carb}}$ , TOC/TS, and Y/Ho ratios of the Fengcheng Formation in the Mahu Sag. A = average, N = number of samples, SD = standard deviation.

Area Proxies	CSR (Wells F20, FN5, FN7, AK1)			TD (Wells F5, FN1, FN14)	MTM (Wells X40, X76, BQ1, B26)
$\delta^{13}\text{C}_{\text{carb}}$ (‰)	1.4–5.8, A = 3.3, N = 28, SD = 1.3			2.0–7.1, A = 4.6, N = 17, SD = 1.49	-3.8–0.8, A = -0.9, N = 11, SD = 1.7
	$P_1f_1$	$P_1f_2$	$P_1f_3$		
	1.1–2.9, A = 2.3, N = 6, SD = 0.49	1.4–3.3, A = 2.3, N = 9, SD = 0.59	3.5–5.8, A = 4.6, N = 13, SD = 0.72		
$\delta^{18}\text{O}_{\text{carb}}$ (‰)	-6–3.4, A = -0.4, N = 28, SD = 2.04			-11.9–3.7, A = -3.7, N = 17, SD = 4.87	-15.3–1.4, A = -8.7, N = 11, SD = 5.1
	$P_1f_1$	$P_1f_2$	$P_1f_3$		
	-2.9–1.6, A = -2.3, N = 6, SD = 0.55	-1.0–1.0, A = 0.3, N = 9, SD = 0.59	-6.0–3.4, A = -0.1, N = 13, SD = 2.57		
Z-value	129–141, A = 134, N = 28, SD = 3.07			126–144, A = 135, N = 17, SD = 4.76	113–129, A = 121, N = 11, SD = 2.12
	$P_1f_1$	$P_1f_2$	$P_1f_3$		
	129–132, A = 131, N = 6, SD = 1.24	130–134, A = 132, N = 9, SD = 1.30	133–141.64, A = 137, N = 13, SD = 2.20		
TOC/TS	0.36–27.89, A = 4.99, N = 28, SD = 7.20			0.07–2.5, A = 0.94, N = 17, SD = 0.74	0.37–156.72, A = 45.87, N = 11, SD = 60.44
	$P_1f_1$	$P_1f_2$	$P_1f_3$		
	0.36–0.81, A = 0.67, N = 6, SD = 0.15	0.55–1.52, A = 0.86, N = 9, SD = 0.29	2.24–27.89, A = 11.10, N = 13, SD = 7.98		
Y/Ho	21.25–34.16, A = 27.21, N = 28, SD = 2.66			27.48–31.71, A = 29.43, N = 17, SD = 1.12	21.68–29.05, A = 26.79, N = 11, SD = 1.82
	$P_1f_1$	$P_1f_2$	$P_1f_3$		
	26.77–28.93, A = 27.95, N = 6, SD = 0.69	25.30–30.83, A = 27.70, N = 9, SD = 1.42	21.25–34.16, A = 26.63, N = 13, SD = 3.47		

**Table 3:**  $\delta^{15}\text{N}$ , C/N, and  $\delta^{13}\text{C}_{\text{org}}$  values of the Fengcheng Formation in the Mahu Sag. A = average, N = number of samples, SD = standard deviation.  $\delta^{15}\text{N}$  is expressed in ‰ versus AIR and  $\delta^{13}\text{C}_{\text{org}}$  is expressed in ‰ versus V-PDB.

Area Proxies	CSR (Wells F20, FN5, FN7, AK1)			TD (Wells F5, FN1, FN14)	MTM (Wells X40, X76, BQ1, B26)
$\delta^{15}\text{N}$ (‰)	13.2–23.9, A = 19.8, N = 28, SD = 2.78			14.6–24.4, A = 20.25, N = 17, SD = 2.12	10.1–18.6, A = 15.0, N = 11, SD = 2.64
	P <sub>1</sub> f <sub>1</sub>	P <sub>1</sub> f <sub>2</sub>	P <sub>1</sub> f <sub>3</sub>		
	21.8–23.9, A = 22.7, N = 6, SD = 0.74	13.2–21.8, A = 19.1, N = 9, SD = 2.96	13.9–21.7, A = 18.8, N = 13, SD = 2.22		
C/N <sub>atom</sub>	19.31–75.33, A = 43.55, N = 28, SD = 13.24			9.9–50.9, A = 36.9, N = 17, SD = 11.76	2.7–68.7, A = 32.4, N = 11, SD = 22.9
	P <sub>1</sub> f <sub>1</sub>	P <sub>1</sub> f <sub>2</sub>	P <sub>1</sub> f <sub>3</sub>		
	32.0–37.6, A = 34.2, N = 6, SD = 2.01	38.0–71.8, A = 53.6, N = 9, SD = 10.43	19.3–75.3, A = 41.6, N = 13, SD = 13.81		
$\delta^{13}\text{C}_{\text{org}}$ (‰)	-30.6–25.7, A = -27.6, N = 28, SD = 1.15			-30.5–26.1, A = -27.7, N = 17, SD = 1.20	-30.1–24.0, A = -27.4, N = 11, SD = 1.76
	P <sub>1</sub> f <sub>1</sub>	P <sub>1</sub> f <sub>2</sub>	P <sub>1</sub> f <sub>3</sub>		
	-27.2–25.9, A = -26.8, N = 6, SD = 0.42	-28.5–26.7, A = -27.8, N = 9, SD = 0.56	-30.6–25.7, A = -28.1, N = 13, SD = 1.40		

**Table 4:** Evolution of the alkaline lake in the Mahu Sag. Z-values and  $\delta^{18}\text{O}_{\text{carb}}$  values, and  $\delta^{15}\text{N}$  data in this table are all average values.  $\delta^{15}\text{N}$  is expressed in ‰ versus AIR.

Area	Strata	Salinity	$\delta^{15}\text{N}$	Carbonates	Evolutionary sequences
CSR	P <sub>1</sub> f <sub>3</sub>	Z =137, $\delta^{18}\text{O}_{\text{carb}}$ = -0.11‰, high salinity	18.84‰	Mg-Ca+ transitional+ Na carbonates	Strong to weak alkalization
	P <sub>1</sub> f <sub>2</sub>	Z =132, $\delta^{18}\text{O}_{\text{carb}}$ =0.28‰, high salinity	19.06‰	Mg-Ca+ transitional+ Na-carbonates	Strong alkalization
	P <sub>1</sub> f <sub>1</sub>	Z =131, $\delta^{18}\text{O}_{\text{carb}}$ = -2.26‰, medium–high salinity	22.71‰	Mg-Ca+ transitional carbonates	Preliminary alkalization
TD	P <sub>1</sub> f <sub>3</sub>	Z =139, $\delta^{18}\text{O}_{\text{carb}}$ = -1.77‰, high salinity	18.92‰	Mg-Ca+ few transitional carbonates	Preliminary alkalization
	P <sub>1</sub> f <sub>2</sub>	Z =134, $\delta^{18}\text{O}_{\text{carb}}$ = -4.11‰, medium salinity	21.45‰	Mg-Ca+ few transitional carbonates	Preliminary alkalization
	P <sub>1</sub> f <sub>1</sub>	Z =129, $\delta^{18}\text{O}_{\text{carb}}$ = -9.64‰, low salinity	20.65‰	Mg-Ca carbonates	Early onset of alkalization
MTM	P <sub>1</sub> f <sub>3</sub>	Z =126, $\delta^{18}\text{O}_{\text{carb}}$ = -9 ‰, low salinity	14.05‰	Mg-Ca carbonates	Early onset of alkalization
	P <sub>1</sub> f <sub>2</sub>	Z =126, $\delta^{18}\text{O}_{\text{carb}}$ = -5.3 ‰, medium salinity	17.18‰	Mg-Ca carbonates	Early onset of alkalization
	P <sub>1</sub> f <sub>1</sub>	Z =116, $\delta^{18}\text{O}_{\text{carb}}$ = -10.47‰, low salinity	14.73‰	Mg-Ca carbonates	Early onset of alkalization